工學博士學位論文

Vapor Phase Synthesis of Mesoporous Organosilica Thin Film in Shallow Trenches and Its Applications for Low-k Materials

좁은 트렌치 내부에 기상으로 제조된
메조기공 유기실리카 박막의 저유전물질로의 응용

2014年 8月

서울大學校 大學院
化學生物工學部
吳 賢 澤

Vapor Phase Synthesis of Mesoporous Organosilica Thin Film in Shallow Trenches and Its Applications for Low-k Materials

by

Hyuntaek Oh

Submitted to the Graduate School of Seoul National University

in Partial Fulfillment of the Requirements

for the Degree of Doctor of Philosophy

August, 2014

Thesis Adviser: Jyongsik Jang

ABSTRACT

The features of integrated circuits (ICs) are reaching the nanoscale due to advancements in semiconductor technology. With such diminution of IC feature sizes, shallow trench isolation (STI) has attracted considerable attention for effective physical and electronic isolation between the walls of the IC. Materials having low dielectric constants (low-k) are required for STI, especially in extremely small circuit fields, because the low-k materials can reduce crosstalk and the resistance/capacitance time delay.

Two methods have been used to fill the trenches with dielectric materials such as silica and polysilazane: chemical vapor deposition (CVD) and a spin-on process. The CVD process can be used to fill a wide (> 50 nm) trench with organosilica. However, when the width of the trench is less than 50 nm, the trench becomes clogged with deposited organosilica before being fully filled. The spin-on method provides a low-k organosilica film in the trench via spin-coating of a sol-gel precursor solution such as tetraethyl orthosilicate (TEOS), methyl trimethoxysilane (MTMS), or perhydropolysilazane. However, shrinkage can occur during formation of the organosilica via a condensation

reaction. Such shrinkage creates voids and causes sloping of the pattern, leading to reduced IC reliability and performance.

Mesoporous silica containing air voids (k = 1) is one of the most promising low-k materials because of its excellent thermal and chemical stabilities. Ueyama and Hillhouse groups recently reported the synthesis of mesoporous silica films on surfaces using vapor phase synthesis (VPS). VPS provides a mesoporous silica film that shrinks less compared to that from sol-gel synthesis because the vaporized precursors are continuously supplied to a surfactant solution. Few studies have been reported concerning surface patterning of silicon wafers with wide (> 130 nm), low-aspect-ratio (L/D < 4) trenches. Moreover, the synthesis of mesoporous silica is difficult to scale-up for commercialization because of its low elastic modulus (< 4 GPa), which could originate from its porous structure. A dielectric material having a high elastic modulus (> 6 GPa) is required to withstand chemical mechanical polishing (CMP), which is used in semiconductor fabrication. The closed pore of mesoporous silica is necessary to stand without defects or pollutions while CMP. Therefore, it is still challenging to develop novel materials to fill shallow

trenches with low-*k* materials.

We report here the VPS of a low-*k*, crack-free, mesoporous organosilica in a shallow nanotrench with 25 nm width and 400 nm depth (aspect ratio : 16). TEOS, bis(trimethoxy-silyl)ethane (BTMSE), Triethoxy fluorosilane (TEFS) were used as the precursors of the mesoporous organosilica. BTMSE played an important role as a crosslinking agent, which improved the elastic modulus. Moreover, BTMSE enlarged the distance between molecules of organosilica and lowered the dielectric constant. TEFS prevented the adsorption of water molecules at surface of synthesized silica and lowered hygroscopicity. Octyltrimethyl-ammonium bromide (OTAB), dodecyltrimethyl-ammonium bromide (DTAB), and cetyltrimethylammonium bromide (CTAB) were selected for the surfactants. Phosphoric acid was used as the catalyst for the condensation reaction that formed the organosilica in shallow trenches.

KEYWORDS: Low-*k* materials; Mesoporous silica; Organosilica; Cationic surfactants; Fluorinated silica; Young's modulus; Hygroscopicity.

STUDENT NUMBER: 2009–21006

List of Abbreviations

AFM : atomic force microscope probe

BET : Brunauer–Emmett–Teller

BJH : Barrett, Joyner, and Halenda

BSE : back scattered electron

BTE : bis(trimethoxyl) ethane

CMP : chemical mechanical polishing

CTAB : cetyltrimethylammonium bromide

DTAB : dodecyltrimethyl-ammonium bromide

FE-SEM : field-emission scanning electron microscope

FIB : focused ion beam

FTIR : Fourier transform infrared spectroscopy

FOS : fluorinated organosilica

FSG : fluorosilicate glass

HPS : Highly porous silica

MOS : mesoporous organosilica

MSF : mesoporous silica film

OTAB : octyltrimethyl-ammonium bromide

PEO : polyethylene oxide

PPO : polypropylene oxide

PSD : pore-size distribution

PSZ : Pure silica zeolites

SAXS : small-angle X-ray scattering

SOG : spin-on glass

STF : silica thin film

TEFS : triethoxy fluoro silane

TEOS : tetraethyl orthosilicate

VPS : vapor phase synthesis

List of Figures

List of Tables

Table of Contents

1. INTRODUCTION

1.1. Background

1.1.1. Low-k dielectrics

1.1.1.1. Low-k materials in IC

Modern computer IC chips are summary of engineering complexity. Since the development of IC chips, the number of transisters on a chip has been exponentially increasing, approximately double with every two years [1-3]. The drift was first discussed by 1965 by Gordon Moore, although the original discussion suggested as doubling the number of devices every year, and now the phenomenon became popularly known as Moore's Law (Figure 1) [4].

Until now, the highlight in scaling feature sizes has been on the maximization of transistor density (Figure 2) [5-7]. All of these are driven by the needs for electrical performance of IC chips. It is recognized, however, that device physics is not the first bottle neck to the continued performance improvement for systems [8,9]. The challenge will be to carry electric power and to control the timing and of the operation. This challenge extends to the physical properties of electric materials, technology and also includes system architecture (Table 1) [10].

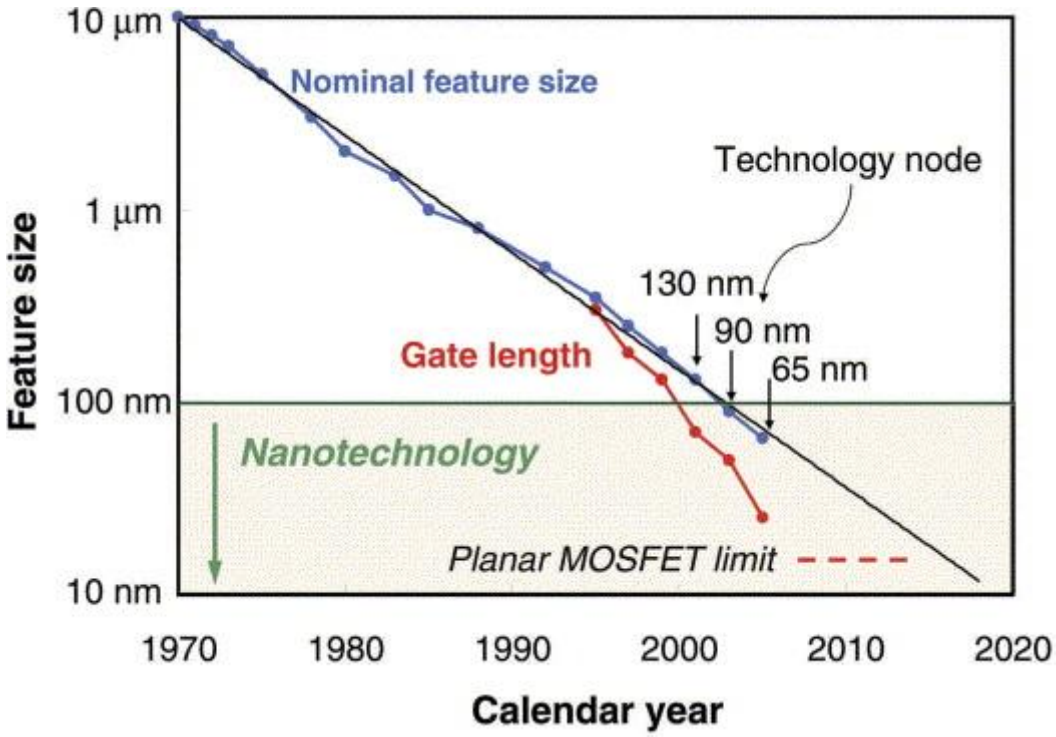

Figure 1. Logic technology node and transistor gate length versus calendar year. Note mainstream Si technology is nanotechnology.

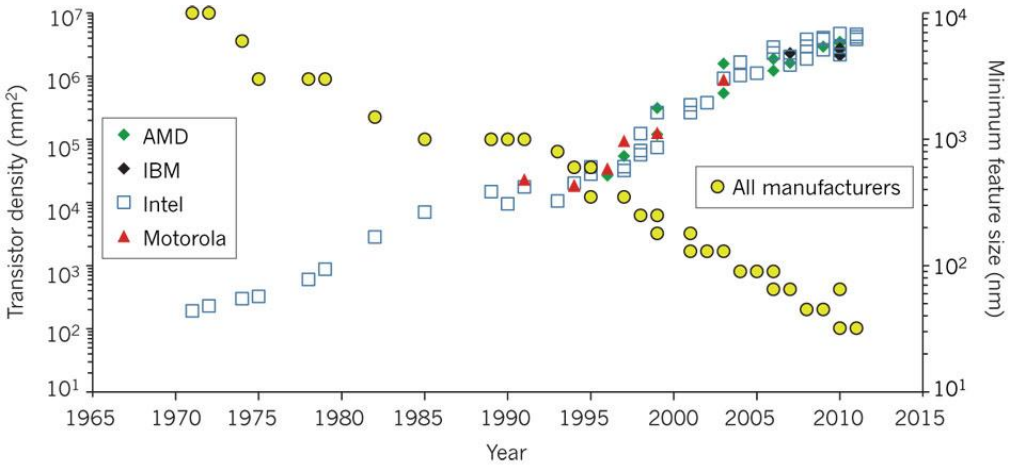

Figure 2. Between 1970 and 2011, the gate length of MOSFETs shrank from 10 μm to 28 nm (yellow circles; *y* axis, right), and the number of transistors per square millimetre increased from 200 to over 1 million (diamonds, triangles and squares show data for the four main microprocessor manufacturers; *y* axis, left).

Table 1. General requirements excepted in low-k materials.

Key performance areas	General requirements
Electrical	Low dielectric constant High breakdown strength High bulk resistance Low DC leakage current
Mechanical	Good adhesion Low stress High hardness
Chemical	Good patternability Low moisture absorption
Thermal	Good thermal conductivity High thermal stability

1.1.1.2. Materials for low-k dielectric application

The first strict meaning of “low-k” dielectric materials was fluorosilicate glass (FSG) (F-SiO_2), also called fluorine-doped oxide which occurred in 2000 with the replacement of conventional SiO_2 for the 180 nm scale trenches [11]. For understanding the scientific principle of superior properties of the material, definition of the dielectric constant of the material by Debye equation is the most important. (Figure 3) [12-14]. With decrease of the bond polarizability of the dielectric by dopping silicon dioxide with fluorine atoms was the preferred method to get the first lower k to <4.0, as required for 180 to 130 nm feature size [15]. FSG had some unique properties that made it the upfront candidate for replacing SiO_2 [16, 17]. The unique properties of FSG were less polaizability compared with conventional SiO_2, strong bond strength (129 Kcal/mol) of Si-F bond, and easy synthesis by CVD methods and sol-gel methods [18].

Meanwhile, polyimides were the first organic polymers to be used into multilayer stacks with Al wiring for electric passivation in the 1980s. They were not strict low-k materials such as FSG, but they could be planarized and watched because of cheap price [19-21]. There have also been reported as multilevel builds with copper electrodes using polyimides interlayer [22]. The extreme thermal stability are required to IC chips application, aromatic

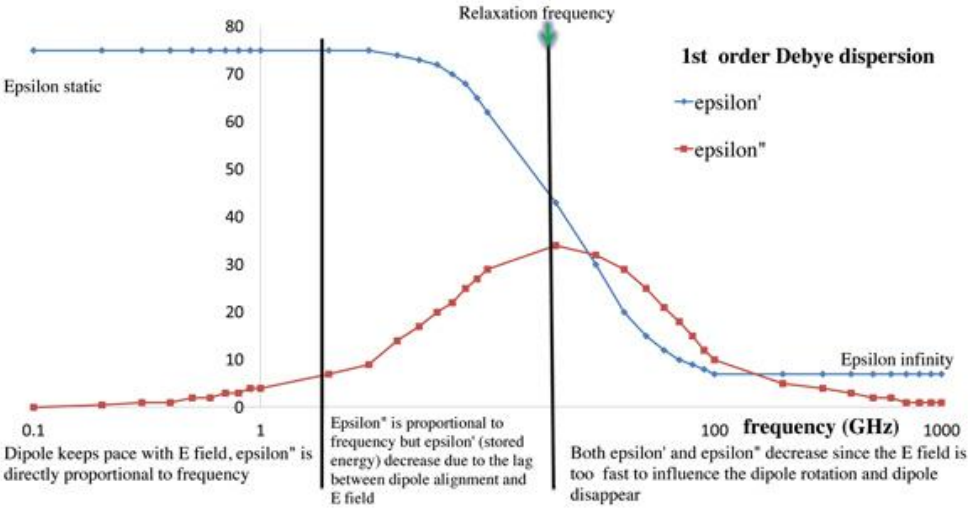

Figure 3. Illustration of Debye dispersion showing a single material relaxation.

substituents in the precursors and polymers [23, 24] are essential. The polyimides are formed from the imide coupling between dianhydrides and diamines, the unique physical properties are originated by these components [25]. In general, polyimides can be produced as rigid, semiflexible, and flexible materials by the flexible portion in their molecular structure including dianhydrides and diamines [26, 27]. Many polyimides including aromatic ring are insoluble in organic solvents, and very few examples can be meltprocessed because of their rigid molecular structure [28]. For this reason, they are conventionally prepared as precursor or prepolymer, and cast as films, and react either by heat or chemically. The initial reaction of a diamine between a dianhydride forms the precursor poly(amic acid), and the precursor is soluble in polar solvents and can be casted into films. After reaction, precursor converted into polyimides by thermal treatment or alternatively by chemical dehydration with acetic anhydride [29, 30].

Many porous polymers are commercially available in electronics. However, there are only few polymers which have uniform nanoscopic pores (<20 nm), stable at thin film (<1000 nm), and satisfy the requirements for on-chip application [31, 32]. To search for such materials, first, it was not surprising that people should use the polyimides for their extensive connection with the microelectronics industry. Many reports described the generation of pores in

polymer using a sacrificial pore generator (porogen) which can be removed thermally [33, 34]. As another example, SiLK is an organic polyarylene thermosetting polymer commercialized by Dow Chemical (Figure 4) [35-37]. Without the introduction of pore, the dielectric constant of SiLK is ～2.6. The low k value for dense SiLK is quite low compared with general dense polyimides and FSG which containing pores [35, 36]. Besides, the physical properties of SiLK are superior to polyimides and FSG. In this point, lower amounts of pore are good for physical properties, and noninterconnected porous morphologies are better than interconnected porosity by porogen for integration purposes (Figure 5) [38].

Pure silica zeolites (PSZs) are microporous (<2 nm) crystalline silica that consist of an open silicate framework consist of SiO_2 tetrahedra molecular structure [39-41]. The first two examples of PSZs appeared in the articles at the end of the 1970s: silicalite- 1 and silicalite-2 [40, 41]. At 2005, 19 species of zeolites had been developed in a pure silica form [42]. Different with conventional aluminosilicate zeolites, PSZs do not contain framework charges originated from semiconducting materials and cations. Therefore, PSZs are detrimental for electronic applications [43]. In addition, a material which containing micropore (< 2 nm) is expected to have better mechanical properties and the pores are significantly smaller than feature size of IC chips [44].

Therefore, many physical properties issues are related to the presence of mesopores, but interconnectivity might still be a challange. As an example, the highly porous films suffer from bad adhesion with silicon wafer, and defects during chemical mechanical polishing (CMP) [45]. Mechanical properties can be restored by a microwave-assisted secondary growth of silicalite in their mesopores. However, the loss of its mesopore leads to an increase of the dielectric constant to a value of 3.0 [46].

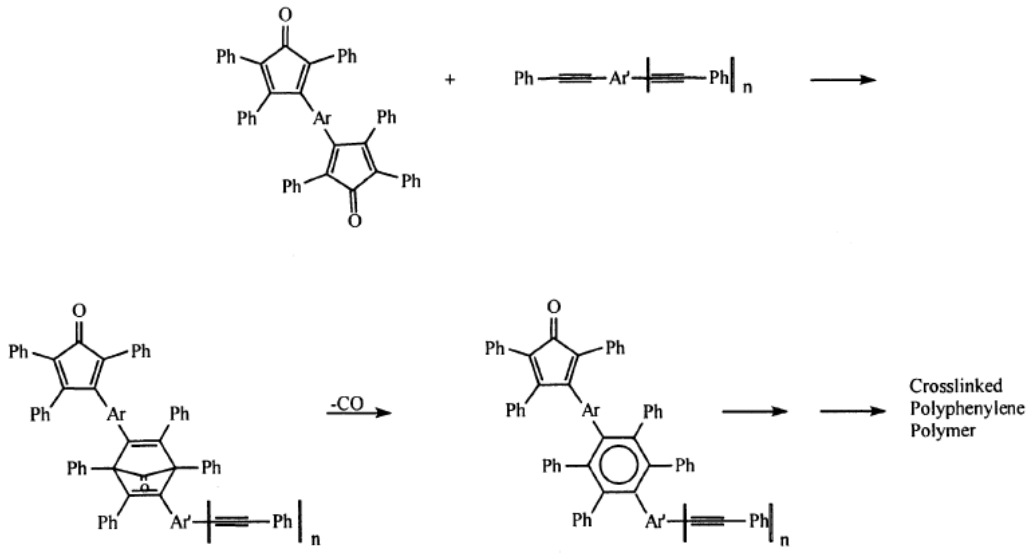

Figure 4. The SiLK polymer structure and polymerization reaction.

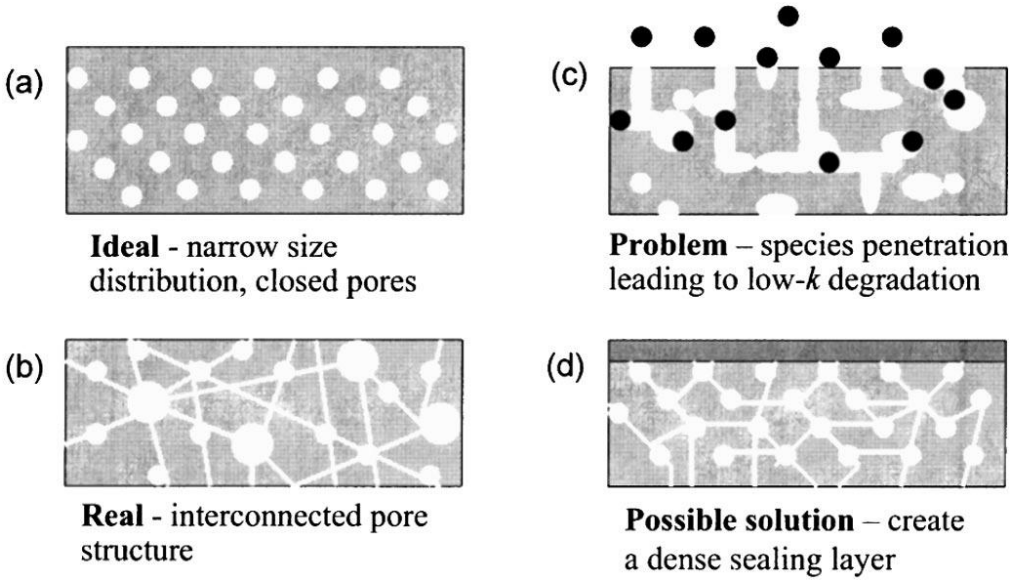

Figure 5. Schematic diagrams of porous low-k dielectric materials showing (a) ideal uniformly dispersed closed pores with a narrow size distribution, (b) interconnected pores with a random size distribution, (c) diffusion and penetration of species into a porous network, and (d) uniformly dispersed interconnected pores with a dense sealing layer

1.1.1.3. Spin-on deposition of low-k dielectrics

The spin-on process is a well known deposition method for dielectric films on substrates [47-49]. It can be introduced for when good planarization and gap fill properties are required. Not only inorganic films, but also organic films can be introduced by spin-on, and their final molecular structure can be either amorphous or crystalline. The precursors for spin-on process should be soluble form or ‘sol’ form (*cf.* a dispersed solution of primary particles/polymers mixed with a solvent) (Figure 6) [50].

Thin film coating is performed by spun up a liquid precursor at the center of the substrate by spin coater. Spin coater is common way for uniform apply of solution on the substrate. Rotation of the substrate induces centrifugal forces that create uniform distribution of material on the surface. The thickness of the coating is influenced by the balance between centrifugal forces (dependent on the rotation speed v) and viscous forces (dependent on the viscosity of the solution) [50]. After the spin coating, the heating or ‘‘bake’’ at temperatures typically below 250 ℃ are used for removal of the residual precursors and solvents. Finally, a sintering at temperatures at 350 to 600 ℃ is performed to obtain a stable film. If the materials have crosslinking agents, in this curing step, the polymer chains are crosslinkged and form the mechanically stable film structure (Figure 7) [51].

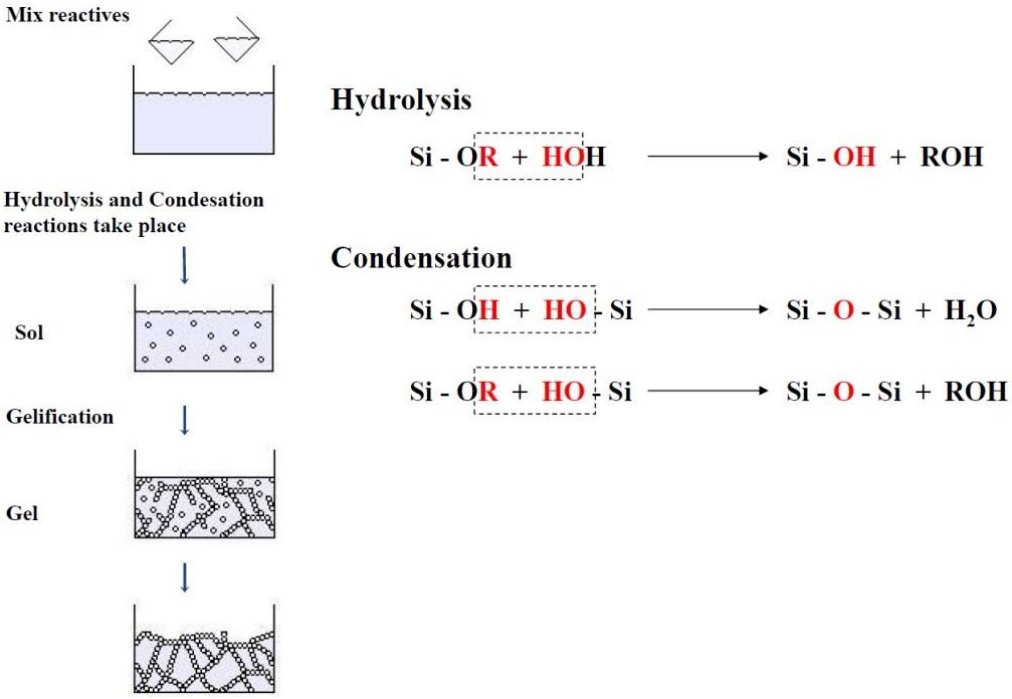

Figure 6. Typical sol-gel process for SiO_2 formation from silicone alkoxide.

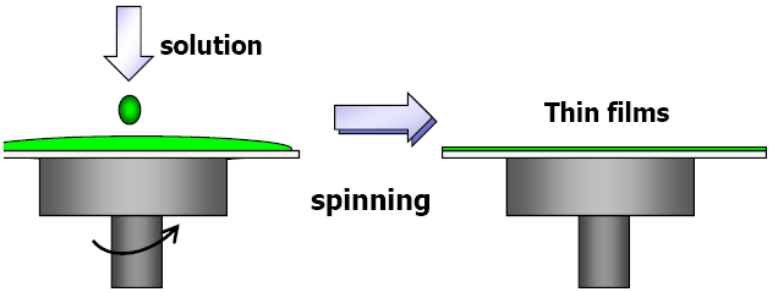

Figure 7. Schematic diagram of typical spin coating process of sol-gel solution containing silica precursors.

Spin-on amorphous dielectric materials with an inorganic backbone are named as spin-on glasses (SOGs). There are various specific sol–gel reactions and they are combinations of hydrolysis of precursors, and condensation processes. The hydrolysis is a transition from Si–OR or Si–R functional groups to Si–OH silanol groups by moisture [51]. After hydrolysis, silanol groups can condensate into a Si–O–Si structure each other, by the elimination of H_2O in their molecular structre.

After spinning, the viscosity of sol increases and sol forms a ‘‘wet gel.’’ The mechanisms at the molecular level explanation for this sudden transition are not perfectly understood [52]. The wet gel is a rigid material which has both liquid and solid components. The solid part is formed by amorphos or crystalline connected precursors, and the liquid fills the free space surrounding the solid part. After the formation of wet gel, the gel is dried at a moderate temperature (<250 ℃, bake). During this bake step, the original solvents and residual precursors are removed and the film loses the most weight and volume loss of up to 50%. For thin films, this shrinkage should be occurred only to the perpendicular direction to the substrate plane. A difference between xerogels and aerogels are made by the special technique for drying. Xerogels are formed by conventional drying by evaporation on the surface, and aerogels are made by supercritical drying of solvents [53].

1.1.1.4. Chemical vapor deposition of low-k dielectrics

The fundamental principles of CVD include a wide variety of scientific and technical principles such as gas-phase reaction chemistry, thermodynamics, surface and plasma reactions, thin film growth mechanism, heat and material transfer, fluid mechanics, and reactors engineering (Figure 8) [54, 55]. Active precursors and structural units such as oligomers are formed in the gas phase, before being introduced in the matrix of the growing layer. A typical example is deposition of silica layers by silane oxidation using active precursor. Active intermediates (SiH_3 , SiH3OH etc.) are formed in the gas phase by thermal initiation and perform chain-branch reaction [56]. The lifetime and concentration of the active intermediates in the gas phase is proportional to the reactor volume (V) and inversely proportional to the internal surface area (S) of the reactor including the wafer surface because the chain-branch reactions are mainly terminated by the surface. If the S/V ratio is too high, all intermediates necessary for film formation are deactivated on the reactor and sample surfaces and no solid product formation is observed [57]. If the S/V ratio is sufficiently small, then concentration of intermediates in the gas phase is too high and further transformations mainly occur via polymerization reactions forming powder like product (aerosyl). Only in the optimal S/V range, a solid film is deposited with a chemical composition close to SiO2, but different structural

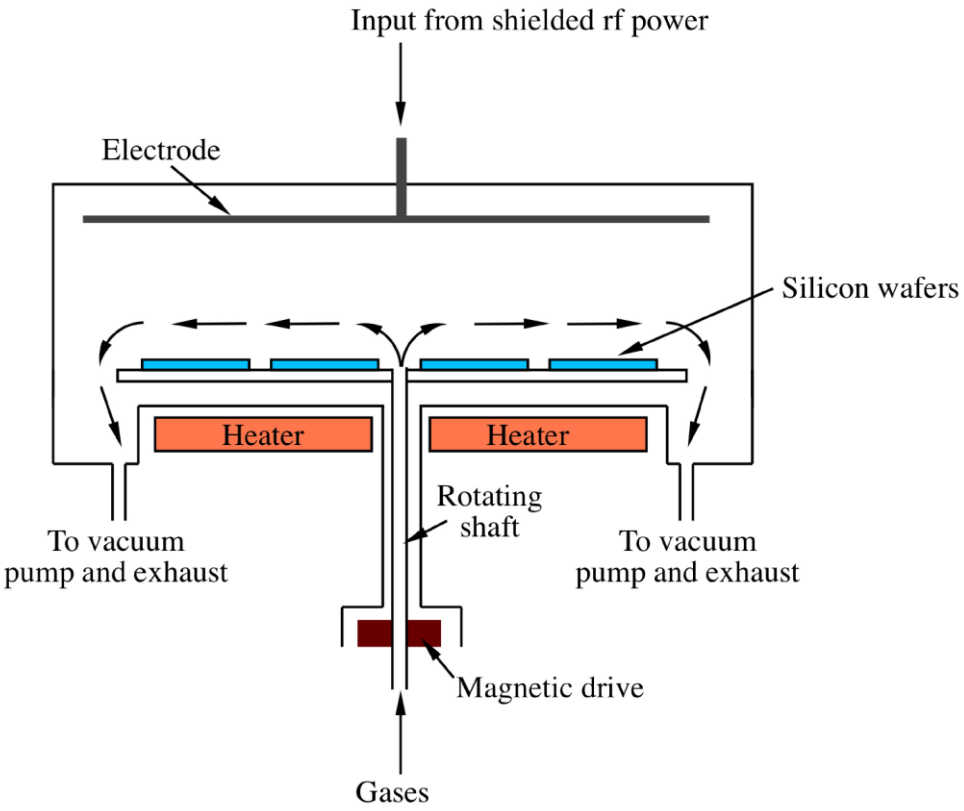

Figure 8. Schematic representation of a radial flow PECVD reactor

groups, which are typical for aerosyl, are also observed ($HOSiO_{3/2}$, $(OH)2SiO_{2/2}$, $HSiO_{3/2}$ etc.) [55]. Therefore, important parameters to achieve constitutive porosity are the S/V ratio, the deposition temperature, and pressure. These parameters define the limits of self-ignition of SiH_4. Selfignition (thermal explosion) represents the rapid increase of reaction rate with temperature for the kinetics of chain - branch exothermic reactions. The acceleration of the reaction rate results in a faster temperature rise upon which the process gets an autocatalytic character. The occurrence of an ignition depends on temperature, pressure, and reactants concentration. Increasing the pressure takes the system through the lower limit of self-ignition [58]. The chain–branch reaction is terminated by the upper limit of self-ignition due to the increase of three-particle collisions in the gas phase. For the case at hand, formation of a solid product occurs inside the self-ignition region in which solid SiO_2 and gas phase H_2O products are formed in a finite range of SiH_4 /O_2 concentrations. Constitutively porous films are formed in conditions close to the region of powder formation.

1.1.2. Characteristics of mesoporous silica

1.1.2.1. Synthesis of Mesoporous silica

Mesoporous silica including MCM-41 and SBA-15 silica have a honeycomb structure and hundreds of empty channels (mesopores) which can absorb or contain small molecules. Mesoporous silica have large surface area (>900 m^2/g), high pore volume (>0.9 cm^3/g), narrow pore size distribution (2–10 nm) [59-61]. Also, mesoporous silica have good thermal and chemical stability originated from stable silica. From first discovery of mesoporos using soft template by surfactants in 1992, various structure or surface functionalization are developed and used for various applications, such as catalysis, drug delivery system, and sensors (Figure 9) [59]. However, conventionally synthesized mesoporous silica have various shapes and pore size. The polydispersity of mesoporous silica is the challenge for usage in many applications.

Unger, Stucky, and Zhao are the first groups which make size controlled mesoporous silica spheres [62-64]. Their goal is to synthesize the particle with homogeneous particle size and monodispersity of mesoporous silica particles for chromatographical applications. Their synthesis procedure of mesoporous silica spheres is based on the Stöber reaction at controlled condition for the synthesis of monodisperse dense silica spheres [59].

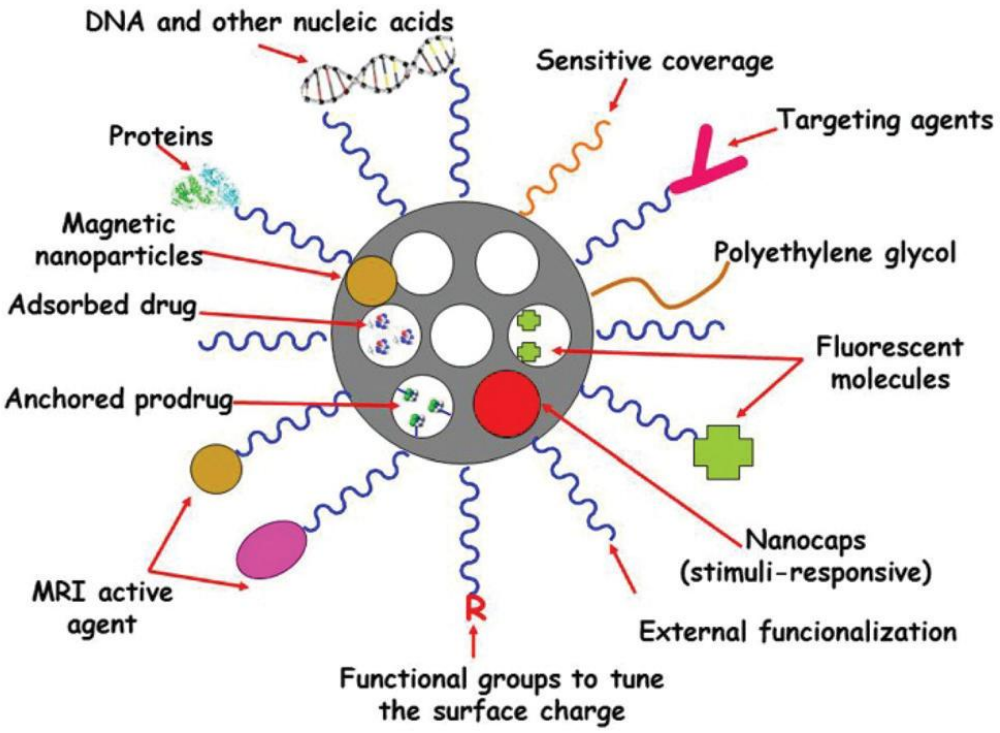

Figure 9. Multifunctionality and cargo loading possibilities of MSNPs. Small drug molecules can be loaded into the mesopores by adsorption from solution.

The reaction is the combination of subsequent hydrolysis and condensation of TEOS. While reaction TEOS was hydrolyzed to silanol by water. After hydrolyzation, aqueous ammonia was catalyst and alkyltrialkoxysilane played a role of structure-directing agent.

On the other hands, many groups tried to synthesize mesoporous silica with homogeneous size and structure by various ways [63]. The homogeneous mesoporous silica could be made by fine tunning of reaction condition such as amount of reactants and concentration of various surfactants [64].

1.1.2.2. Mesoporous silica as low-k dielectric

Mesoporous silica has lately attracted considerable attention for usage of low-k dielectric material for advanced IC chips (Figure 10) [65]. There was two ways for synthesis of mesoporous silica thin films for low-k dielectric. First, mesoporous silica thin films were synthesized using solution precursors by aerogel process including controlled gelation and removal of solvents such as water and alcohol. The other way was synthesis by soft template using structure-directing agents such as alkyltrialkoxysilane or surfactants and removal of them after the reaction [65, 66].

General solvents for sol-gel reaction including water and alcohol are not suitable for drying. Therefore, supercritical fluids such as CO_2 (Tc=31 ℃, Pc=1050 psi) are used to make aerogel after solvents exchange [65]. Aerogels have mesoporus structure with random pore size because the drying while reaction is not controllable. However, aerogel based mesoporous silica are still of interest because of its very low dielectric constant and tunable physical properties.

There were numerous articles for mesoporous materials by sol-gel process. They showed various synthesize procedure, reaction conditions, and many applications of the mesoporous silica. However, there are few commercialized applications exclude catalyst or biological applications [67-69].

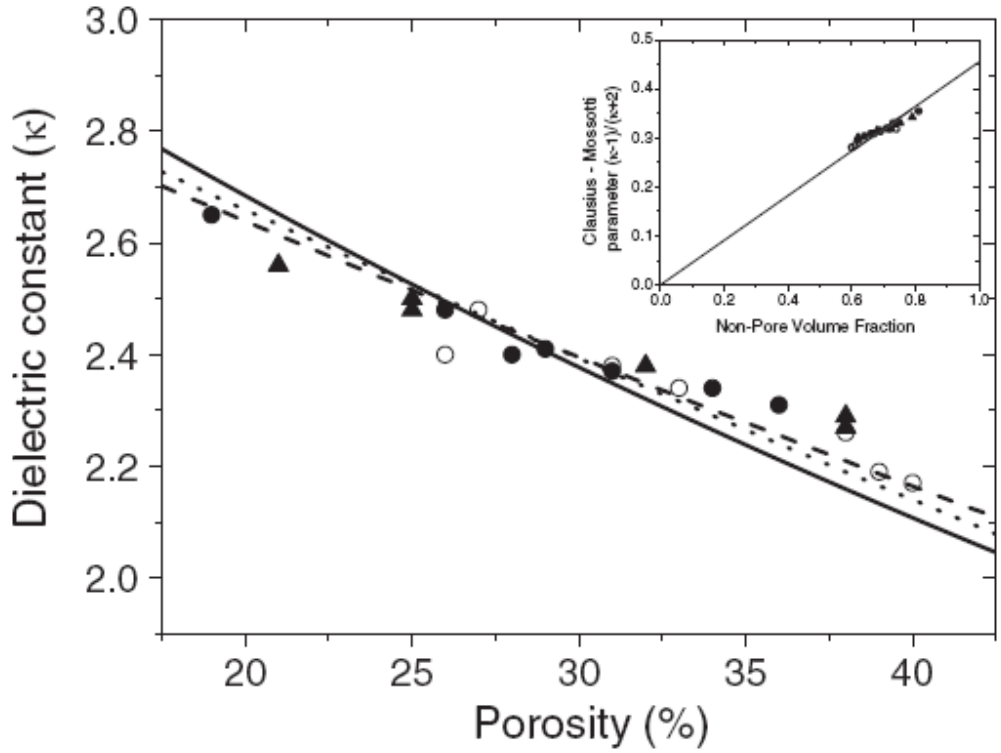

Figure 10. Evolution of the dielectric constant as function of the porosity for porous SiOCH films deposited with different porogen loading using ● DEMS and NBD at 300 °C then cured using UV ○ DEMS and NBD at 300 °C then cured using a thermal treatment and ▲ DEMS and ATRP at 260 C then cured using UV. Several mixing rules are also plotted: _ _ _ Maxwell – Garnett, ... Bruggeman and ____ Lorentz-Lorenz equations. The inset shows the variation of the Clausius-Mossotti parameter as function of the porosity.

One of the most recent applications of mesoporus silica is for dielectric material. For application of dielectric material, not only good physical properties, but also easy tenability is required. The physical properties of mesoporous silica are easy controllable in both of areogel and sol-gel process [70].

1.2. Objectives and Outline of the Study

1.2.1. Objectives

In the preceding section, the importance of mesoporous silica in low-k dielectric material was introduced from the viewpoint of academic research and practical applications. The aim of this dissertation is to present new synthetic methodology for mesoporous silica in nanosized trench and its distinguished physical properties. Furthermore, the physical properties of synthesized mesoporous silica were modified by various precursors which played roles as crosslinking agent and moisture-proof precursor.

1.2.2. Outline

This dissertation involves the following subtopics:

I. Vapor Phase Synthesis of Silica Thin Film in shallow trench
   1. Fabrication of Dense Silica Thin Film for Shallow trench Isolation
   2. Preparation of Mesoporous Silica in Shallow Trench using Cationic Surfactants and Vaporized Precursor
   3. Synthesis of highly porous silica in shallow trench for low-k application

II. Fabrication of Modified Mesoporous Silica with Enhanced Physical Properties for Low-k applications
   1. Elastic Modulus Modification of Mesoporous Silica Using Crosslinking

Agent

2. Fabrication of Mesoporous Organosilica Film with Enhanced Physical Properties Using Sol-gel Process and Vapor Phase Synthesis
3. Hygroscopicity Modification of Mesoporous Silica Using Fluorinated Silane Coupling Agent

A detailed outline of the study is as follows:

1. Vapor phase synthesis of TEOS has offered defect-less gap filling of silica in shallow trenches. Generally, Sol-gel methods and PECVD methods are used for shallow trench isolation with functionalized silica. However, sol-gel methods accompany volume reduction because of condensation while reactions, and occur shrinkage. PECVD can be used for shallow trench isolation in only over 100 nm scale of trenches. In under 100 nm scale, the trenches are clogged by deposited precursors and the voids are occurred in trenches. Although much attention has been paid to study of them, they are still challenging.

   In this dissertation, the silica thin film (STF) is successfully synthesized on nanopatterned silicon wafer using catalyst solution and vaporized precursor. The vapor phase synthesis is used to synthesize silica without defects which originated from shrinkage while sol-gel reaction.

The surface of synthesized STF is smooth and the nanopattern is not able to obsearve because of STF. Also, the silica fills the shallow trenches with 25 nm width and 400 nm depths. The cross-sectional images are obtained by SEM and TEM using FIB and they proof gap filling of shallow trenches by STF without significant defects. This novel strategy offers great possibility for fabricating low-k dielectric based on various precursors that has tunable physical properties.

2. Mesoporous materials have attracted a great deal of interest as the most promising low-k dielectrics. Air voids with very low dielectric constant (k=1) in mesoporous materials lower dielectric constant of entire dielectric materials. Among mesoporous materials, mesoporous silica has many advantages such as low chemical reactivity, high porosity and ease to synthesize.

   In this dissertation, the mesoporous silica film (MSF) is successfully synthesized on nanopatterned silicon wafer using surfactant solution and vaporized precursor. The vapor phase synthesis is used to synthesize silica without defects which originated from shrinkage while sol-gel reaction. The surface of synthesized MSF is smooth and the nanopattern is not able to obsearve because of STF. Also, the silica fills the shallow trenches with 25 nm width and 400 nm depths. The cross-sectional images are obtained

by SEM and TEM using FIB and they proof gap filling of shallow trenches by STF without significant defects. The lamellar mesoporous structure is observed at TEM images. BET measurement is employed to analysis porosity and dielectric constant of MOS, and it has extremely low dielectric constant.

3. Though mesoporous silica have many advantages for usage as low-k dielectrics, it is very hard to use in industrial manufacturing process. This is because of weak mechanical property due to high porous structure and loose molecular structure. To overcome these problems, closslinking agents are employed.

   In this dissertation, a silane coupling agent (BTE) which can play a role of crosslinking agent is introduced in vapor phase synthesis. BTE can be vaporized and hydrolyzed at the surface of surfactants solution. Two precursors, TEOS and BTE, form the crosslinked organosilica complex. Crosslinked organosilica has relatively higher elastic modulus and lower dielectric constant than the MOS without crosslinking agent.

4. In practical IC chips, chemical mechanical polishing (CMP) process is performed to planarization after deposition of dielectric layer. Therfore, the moisture can penetrate dielectric layer while from CMP process before packaging. Compared with conventional low-k dielectric, mesoporous

silica can adsorb moisture because of its high porosity. To overcome this problem, fluorinated silica coupling agent is used as co-precursor.

In this dissertation, fluorinated silane coupling agent (TEFS) can play a role of lower hygroscopy of synthesized MOS. TEFS can be easily vaporized and hydrolyzed at the surface of surfactants solution. Two precursors, TEOS and TEFS, form the organosilica complex. Synthesized MOS has lower moisture absorptivity and lower dielectric constant compared with pristine MOS.

2. EXPERIMENTAL DETAILS

2.1. Vapor Phase Synthesis of Silica Thin Film in Shallow Trench

2.1.1. Fabrication of Dense Silica Thin Film for Shallow trench Isolation

The nanopatterned silicon wafers were prepared by 2-step ArF (193 nm) immersion lithography and 2-step dry etching. The following chemicals were purchased and used as received: phosphoric acid (Samchun chemical), absolute ethanol (Samchun chemical), and tetraethyl orthosilicate (Aldrich).

The catalyst solution is composed of absolute ethanol (1.15 g), distilled water (9 g), and phosphoric acid (85 wt%, 1 g). The catalyst solution was filtered by syringe filter with average pore diameter of 200 nm to remove impurities before use.

Nanopatterned silicon wafer was cleaned by a hot mixture of ethanol/acetone (1:1) for 1 h. The wafer was quickly taken out from washing solution at hot condition to prevent collapse of pattern by surface tension while slow drying and condensation of water. After washing, the nanopatterned silicon wafer was modified with O_2 plasma for 30 s with 20 sccm of gas flow rate and 100 W power to provide hydrophilicity on its surface. The wafer was immersed in the catalyst solution for 5 min and spun up with 3000 rpm for 30 s by spin coater to make uniform coating on surface and remove excess solution.

After spin coating, the wafer was placed into closed vessel that was saturated with vaporized TEOS. For saturation of precursors, the vessel was pre-heated by convection oven at 70 ℃ for 30 min. Vaporized precursors were permeated and diffused into catalyst solution, and vapor phase synthesis for the silica thin film (STF) was performed in the vessel at 70 ℃ for 12 h. Finally, the wafer was washed by absolute ethanol to remove phosphoric acid and residual precursor. After washing, the wafer was calcined at 500 ℃ for 2 h in the air for sintering and to remove solvent and excess precursor.

Surface FE-SEM images were taken by JEOL JSM-6701F at an acceleration voltage of 10 kV. For SEM measurement, Pt/Pd alloy was sputtered on all STF samples (bare Si wafer was used without sputtering) by Cressington 108 auto sputter coater at 20 mA for 120 s. Cross-sectional FE-SEM images were collected by Carl Zeiss auriga at an acceleration voltage of 20 kV. For elemental mapping image, back scattered electrons (BSE) mode and FIB module were used. TEM images were obtained using JEOL JEM-2100 at an acceleration voltage of 200 kV. SII nanotechnology SMI3050SE was used for focused ion beam (FIB). Elastic modulus was obtained using nano-indentation by VEECO INNV-BASE.

2.1.2. Preparation of Mesoporous Silica in Shallow Trench using Cationic Surfactants and Vaporized Precursor

The nanopatterned silicon wafer (width: 25 nm, height: 400 nm) was prepared by 2-step ArF (193 nm) immersion lithography and 2-step dry etching. The following chemicals were purchased and used as received: Octyltrimethyl-ammonium bromide (OTAB) (TCI Korea), dodecyltrimethyl-ammonium bromide (DTAB) (TCI Korea), cetyltrimethylammonium bromide (CTAB) (TCI Korea), hydrochloric acid (Samchun chemical), absolute ethanol (Samchun chemical), and tetraethyl orthosilicate (Aldrich).

The surfactants solutions were composed of cationic surfactants, HCl, absolute ethanol and distilled water. The amount of solutions included 0.15 g, 1.15 ml, and 9 ml of HCl, absolute ethanol, and water, respectively. 3.76 mmol of CTAB, DTAB, and OTAB (1.37 g, 1.15 g, 0.88 g, respectively) were used to form micellar structure.

The nanopatterned silicon wafer was prepared by argon floride emulsion lithography and 2-step dry etch, and it was used as substrate. Firstly, the wafer was treated with O2 plasma for 1 min with 20 sccm of gas flow rate and 100 W power to provide affinity with aqueous surfactant solution. In case of MOS-16, the plasma treated wafer was soaked into the sufficient amount of surfactant solution composed of CTAB, HCl and distilled water for 5 min. The CTAB

was self-assembled on the surface of wafer and the lamellar structured micelles were formed. The cationic heads of CTAB faced to the surface of wafer because of charge-charge interaction between the nitrogen atom of CTAB and hydroxyl groups of plasma treated wafer. After 5 min soaking, the wafer was taken out from aqueous surfactant solution, and was spun up with 5000 rpm by spin coater for 30 s to remove excess surfactant solution. Then, the wafer was moved into a closed vessel containing vaporized TEOS and BTMSE (molar ratio=9:1) at 70 ℃ for 30 min. The vaporized reagents were continously diffused into nanogap filled with surfactant micelles. The VPS was performed for 12 h in order to form organosilica. The wafer that filled with synthesized MOS was obtained by venting the reactor to isolate from residual reagent vapor. The wafer was calcined to produce the molecular structure of MOS-16 and remove CTAB at 500 ℃ in air for 5 h. The calcined sample was coated on silicon wafer, and it was gathered for characterization including TEM and XRD. In addition, MOS-8, MOS-12 were also prepared using surfactant solution containing same amount of OTAB, DTAB as a substitute of CTAB, repectively.

Surface FE-SEM images and energy-dispersive X-ray spectroscopy (EDS) were taken by JEOL JSM-6701F at an acceleration voltage of 10 kV. For SEM measurement, Pt/Pd alloy was sputtered on all POS samples (bare Si wafer was

used without sputtering) by Cressington 108 auto sputter coater at 20 mA for 120 s. Cross-sectional FE-SEM images were collected by Carl Zeiss auriga at an acceleration voltage of 20 kV. For elemental mapping image, back scattered electrons (BSE) mode and FIB module were used. TEM images were obtained using JEOL JEM-2100 at an acceleration voltage of 200 kV. SII nanotechnology SMI3050SE was used for focused ion beam (FIB). The nitrogen adsorption/desorption isotherm was calculated by the Barrett, Joyner, and Halenda (BJH) method and measured by Micromeritics ASAP 2000 at 77 K. Elastic modulus was obtained using nano-indentation by VEECO INNV-BASE.

2.1.3. Synthesis of highly porous silica in shallow trench for low-*k* application

The nanopatterned silicon wafer (width: 25 nm, height: 400 nm) was prepared by 2-step ArF (193 nm) immersion lithography and 2-step dry etching. The detailed process is described eleswhere. The following chemicals were purchased and used as received: phosphoric acid (Samchun chemical), absolute ethanol (Samchun chemical), and tetraethyl orthosilicate (Aldrich). Cationic surfactant cetyltrimethylammonium bromide was supplied by TCI Korea, and nonionic surfactant pluronic F127 (PEO_{100}-PPO_{65}-PEO_{100}) was provided from BASF.

The surfactant solution is composed of CTAB (1.37 g), F127 (2 g), absolute ethanol (1.15 g), distilled water (9 g), and phosphoric acid (70 wt%, 0.3 g). After mixing of the surfactant solution, it was stirred vigorously for 1 h and aged for 24 h. The surfactant solution was filtered by syringe filter with average pore diameter of 200 nm to remove impurities before use.

The nanopatterned silicon wafer was modified with O_2 plasma for 30 s with 20 sccm of gas flow rate and 100 W power to provide hydrophilicity on its surface. The wafer was immersed in the surfactant solution for 5 min and spun up with 5000 rpm for 30 s by spin coater to make uniform coating on surface and remove excess solution. After spin coating, the wafer was placed into

closed vessel that was saturated with vaporized TEOS. For saturation of precursors, the vessel was pre-heated by convection oven at 90 ℃ for 30 min Vaporized precursors were permeated and diffused into surfactant solution, and vapor phase synthesis was performed in the vessel at 70 ℃ for 12 h. Finally, the wafer was calcined at 500 ℃ for 2 h in the air to remove surfactants, solvent, and excess precursors.

Surface FE-SEM images and energy-dispersive X-ray spectroscopy (EDS) were taken by JEOL JSM-6701F at an acceleration voltage of 10 kV. For SEM measurement, Pt/Pd alloy was sputtered on all POS samples (bare Si wafer was used without sputtering) by Cressington 108 auto sputter coater at 20 mA for 120 s. Cross-sectional FE-SEM images were collected by Carl Zeiss auriga at an acceleration voltage of 20 kV. For elemental mapping image, back scattered electrons (BSE) mode and FIB module were used. TEM images were obtained using JEOL JEM-2100 at an acceleration voltage of 200 kV. SII nanotechnology SMI3050SE was used for focused ion beam (FIB). The nitrogen adsorption/desorption isotherm was calculated by the Barrett, Joyner, and Halenda (BJH) method and measured by Micromeritics ASAP 2000 at 77 K. Elastic modulus was obtained using nano-indentation by VEECO INNV-BASE.

2.2. Fabrication of Modified Mesoporous Silica with Enhanced Physical Properties for Low-*k* applications

2.2.1. Elastic Modulus Modification of Mesoporous Silica Using Crosslinking Agent

The following chemicals were purchased and used as received: phosphoric acid (Samchun chemical), absolute ethanol (Samchun chemical), tetraethyl orthosilicate (Aldrich), and bis(trimethoxy-silyl)ethane (BTE) (Aldrich). Cationic surfactant cetyltrimethylammonium bromide was supplied by TCI Korea.

The surfactants solutions were composed of CTAB, phosphoric acid, absolute ethanol and distilled water. The solutions included 0.3 ml, 1.15 ml, and 9 ml of phosphoric acid, absolute ethanol, and water, respectively. 3.76 mmol of CTAB (1.37 g) were used to form micellar structure. The surfactants solution was filtered by syringe filter with average pore diameter of 200 nm to remove impurities before use.

Pristine silicon wafer was cleaned by a hot mixture of ethanol/acetone (1:1) for 1 h. After washing, the silicon wafer was modified with O_2 plasma for 30 s with 20 sccm of gas flow rate and 100 W power to provide hydrophilicity on its surface. The wafer was immersed in the catalyst solution for 5 min and spun up with 3000 rpm for 30 s by spin coater to make uniform coating on surface and remove excess solution. After spin coating, the wafer was placed into

closed vessel that was saturated with vaporized TEOS and BTE. For saturation of precursors, the vessel was pre-heated by convection oven at 90 ℃ for 2 h. Vaporized precursors were permeated and diffused into catalyst solution, and vapor phase synthesis for the silica thin film (STF) was performed in the vessel at 70 ℃ for 12 h. Finally, the wafer was washed by absolute ethanol to remove phosphoric acid. After washing, the wafer was calcined at 500 ℃ for 2 h in the air for sintering and to remove excess surfactants and precursors. The calcined sample was coated on silicon wafer, and it was gathered for characterization including TEM.

Surface FE-SEM images and energy-dispersive X-ray spectroscopy (EDS) were taken by JEOL JSM-6701F at an acceleration voltage of 10 kV. For SEM measurement, Pt/Pd alloy was sputtered on all STF samples (bare Si wafer was used without sputtering) by Cressington 108 auto sputter coater at 20 mA for 120 s. TEM images were obtained using JEOL JEM-2100 at an acceleration voltage of 200 kV. SII nanotechnology SMI3050SE was used for focused ion beam (FIB). Elastic modulus was obtained using nano-indentation by VEECO INNV-BASE.

2.2.2. Fabrication of Mesoporous Organosilica Film with Enhanced Physical Properties Using Sol-gel Process and Vapor Phase Synthesis

The following chemicals were purchased and used as received: phosphoric acid (Samchun chemical), absolute ethanol (Samchun chemical), tetraethyl orthosilicate (Aldrich), and bis(trimethoxy-silyl)ethane (BTE) (Aldrich). Cationic surfactant cetyltrimethylammonium bromide was supplied by TCI Korea.

The sol-gel solutions were composed of CTAB, phosphoric acid, absolute ethanol, distilled water and silica precursors (TEOS and BTE). First, surfactants solution included 1.37 g, 0.3 ml, and 10 ml of CTAB, phosphoric acid and absolute ethanol, respectively. 3.76 mmol of CTAB (1.37 g) were used to form micellar structure. After mixing of reagents, TEOS and BTE were injected into catalyst solution and used immediately. The sol-gel solution was filtered by syringe filter with average pore diameter of 200 nm to remove impurities before use.

Pristine silicon wafer was cleaned by a hot mixture of ethanol/acetone (1:1) for 1 h. After washing, the silicon wafer was modified with O_2 plasma for 30 s with 20 sccm of gas flow rate and 100 W power to provide hydrophilicity on its surface. The wafer was immersed in the catalyst solution for 5 min and spun up with 1500 rpm for 15 s by spin coater to make uniform coating on surface

and remove excess solution. After spin coating, the wafer was placed into closed vessel that was saturated with vaporized TEOS and BTE. For saturation of precursors, the vessel was pre-heated by convection oven at 90 ℃ for 2 h. Vaporized precursors were permeated and diffused into sol-gel solution, and vapor phase synthesis for the silica thin film (STF) was performed in the vessel at 70 ℃ for 12 h. Finally, the wafer was washed by absolute ethanol to remove phosphoric acid. After washing, the wafer was calcined at 500 ℃ for 2 h in the air for sintering and to remove excess surfactants and precursors. The calcined sample was coated on silicon wafer, and it was gathered for characterization including TEM and XRD.

Surface FE-SEM images and energy-dispersive X-ray spectroscopy (EDS) were taken by JEOL JSM-6701F at an acceleration voltage of 10 kV. For SEM measurement, Pt/Pd alloy was sputtered on all STF samples (bare Si wafer was used without sputtering) by Cressington 108 auto sputter coater at 20 mA for 120 s. TEM images were obtained using JEOL JEM-2100 at an acceleration voltage of 200 kV. SII nanotechnology SMI3050SE was used for focused ion beam (FIB). Elastic modulus was obtained using nano-indentation by VEECO INNV-BASE.

2.2.3. Hygroscopicity Modification of Mesoporous Silica Using Fluorinated Silane Coupling Agent

The following chemicals were purchased and used as received: phosphoric acid (Samchun chemical), absolute ethanol (Samchun chemical), tetraethyl orthosilicate (Aldrich), and triethylflouorosilane (TEFS) (Aldrich). Cationic surfactant cetyltrimethylammonium bromide was supplied by TCI Korea.

The catalyst solution is composed of absolute ethanol (1.15 g), distilled water (9 g), and phosphoric acid (85 wt%, 0.3 g). The catalyst solution was filtered by syringe filter with average pore diameter of 200 nm to remove impurities before use.

Pristine silicon wafer was cleaned by a hot mixture of ethanol/acetone (1:1) for 1 h. After washing, the silicon wafer was modified with O_2 plasma for 30 s with 20 sccm of gas flow rate and 100 W power to provide hydrophilicity on its surface. The wafer was immersed in the catalyst solution for 5 min and spun up with 3000 rpm for 30 s by spin coater to make uniform coating on surface and remove excess solution. After spin coating, the wafer was placed into closed vessel that was saturated with vaporized TEOS and TEFS. For saturation of precursors, the vessel was pre-heated by convection oven at 70 ℃ for 30 min. Vaporized precursors were permeated and diffused into catalyst solution, and vapor phase synthesis for the silica thin film (STF) was

performed in the vessel at 70 ℃ for 12 h. Finally, the wafer was washed by absolute ethanol to remove phosphoric acid. After washing, the wafer was calcined at 500 ℃ for 2 h in the air for sintering and to remove excess surfactants and precursors. The calcined sample was coated on silicon wafer, and it was gathered for characterization including FT-IR and TGA.

Surface FE-SEM images and energy-dispersive X-ray spectroscopy (EDS) were taken by JEOL JSM-6701F at an acceleration voltage of 10 kV. For SEM measurement, Pt/Pd alloy was sputtered on all STF samples (bare Si wafer was used without sputtering) by Cressington 108 auto sputter coater at 20 mA for 120 s. TEM images were obtained using JEOL JEM-2100 at an acceleration voltage of 200 kV. SII nanotechnology SMI3050SE was used for focused ion beam (FIB). Elastic modulus was obtained using nano-indentation by VEECO INNV-BASE.

3. Results and Discussion

3.1. Vapor Phase Synthesis of Silica Thin Film in shallow trench

3.1.1. Fabrication of Dense Silica Thin Film for Shallow trench Isolation

In order to satisfy the strict performance requirement of insulating materials, many precursors and processed were developed to optimizing physical properties such as dielectric constant, elastic modulus, and perfect gap-filling in shallow trenches [71-73]. We report here the novel process for gap-filling of shallow trenches by silica with remarkable physical properties using vapor phase synthesis (VPS). The precursor for silica thin film (STF) was TEOS and phosphoric acid was used as catalyst. Vaporized TEOS was introduced into catalyst solution which containing phosphoric acid, and formed STF in shallow trenches.

The overall synthesis of the POS in shallow trenches of a patterned wafer is illustrated in Figure 11. First, the patterned wafer was treated with O2 plasma for 1 min with 20 ccm of gas flow and 100 W power to hydrophilicity on surface. The plasma treated wafer was soaked in catalyst solution containing

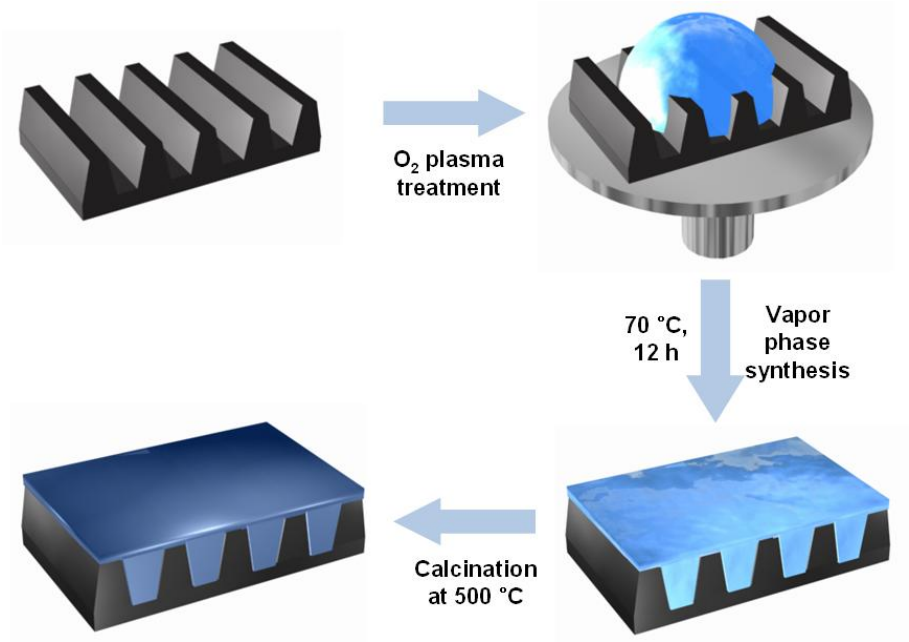

Figure 11. Schematic illustration of the fabrication of mesoporous silica thin film using VPS in a shallow trench.

phosphoric acid. After 5 min soaking, shallow trenches were filled with catalyst solution because of hydrophilic surface. The wafer was taken out from catalyst solution, and was spin coated at 1500 rpm for 15 s to remove excess catalyst solution. Before reaction, precursor was vaporized in a vessel at 70 ℃ for 1 h. The wafer was taken in the vessel that saturated with vaporized precursor. Vaporized precursor was hydrolyzed to silanol from surface of spin coated catalyst solution at 70 ℃ for 12 h. Hydrolyzed precursor diffused to entire solution, and reacted with catalyst. The reaction of precursor was condensation reaction. After reaction, the wafer was calcined at 500 ℃ for 2 h to remove excess reagents.

Figure 12 displays field-emission scanning electron microscope (FE-SEM) images of surface of the pristine wafer and the STF coated wafer. The FE-SEM images clearly show that the trenches of the pristine wafer were covered with synthesized silica. In figure 12a, the wafer has vertically aligned shallow trenches and the width and feature size of them were 25 nm and 25 nm, respectively. There were no significant defects at trenches what were originated from pre-treatment such as cutting, plasma treatment, and washing. Figure 12b shows surface of the wafer after reaction. The nanopattern was fully covered with STF and trenches were could not be observed with perpendicular viewpoint. STF had smooth surface and there was no significant defects such

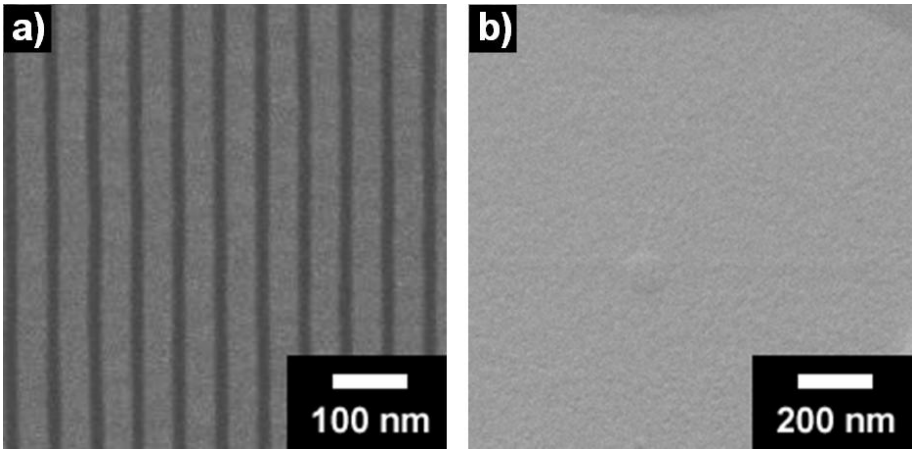

Figure 12. Surfacial FE-SEM images of a) bare patterned silicon wafer b) the STF filled patterned Si wafer.

as crack and distortion.

The cross-sectional FE-SEM images of pristine and STF-filled wafer (Figure 13) show the STF which is filling shallow trenches. The pristine wafer had thin walls and reverse-triangle-shaped trenches (Figures 13a) with a width, depth, and feature size of 25 nm, 400 nm, and 25 nm, respectively. After the vapor phase synthesis, shallow trenches of the wafer were filled with synthesized STF (Figure 13b). The images were investigated using focused ion beam (FIB) and back scattered electrons (BSE) detector. FIB method could etch the wafer vertically by gallium ion and enabled to observe the section of sample [74]. After vertical etching, silicon and silica in the section of sample could not be distinguished because they had same height. However, BSE detector could distinguish silicon and silica by the numbers of components atoms. In BSE detector, heavier atoms appear brighter than lighter atoms. As can be seen at Figure 3b, STF appears darker than the silicon wafer because it contains atoms that are lighter than silicon, *i.e.*, carbon and oxygen [75, 76]. Significant defects such as crack, leaning, and void were not observed in cross-sectional SEM image. Therefore, STF was successfully synthesized in shallow trenches without defects.

To observe the detailed structure of STF filled wafer, cross-sectional TEM image was obtained using FIB. The trench after VPS is illustrated in

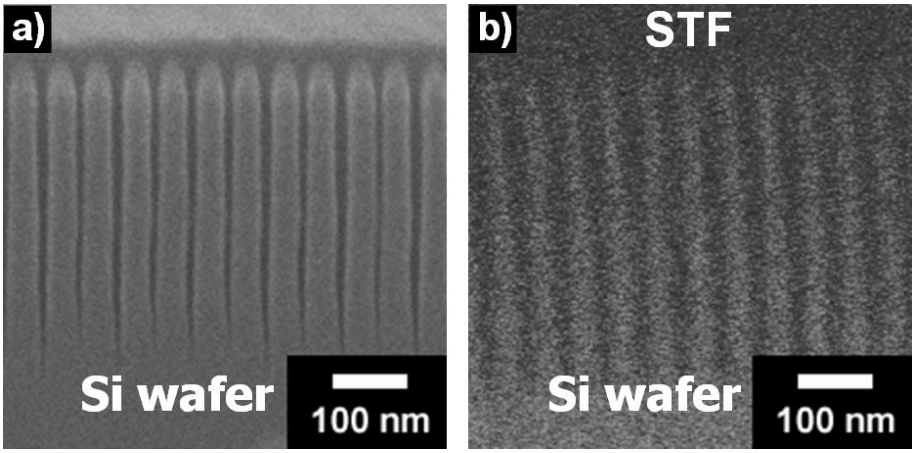

Figure 13. Cross-sectional FE-SEM images of a) bare patterned silicon wafer b)the STF filled patterned Si wafer.

Figure 14a. STF was observed at the shallow trenches and the surface of patterned wafer. The morphology of STF was uniform from the wide top to the narrow bottom of the trenches without defects. It indicated that the vaporized precursors could be penetrated into the surfactant solution and the STF was formed *via* a condensation reaction [77]. High-magnification TEM images (Figure 14b, c) demonstrated that the structures of the STF in the trenches were crack-free. No significant cracking or leaning occurred from the top to the bottom of trenches. The plasma treatment provided hydroxyl groups on the surface of the silicon wafers, and these functional groups formed chemical bonding with the silicon atoms in TEOS [78, 79]. Judging from these data, vapor phase synthesis could fabricate the silica in nanosized shallow trenches in silicon wafer, and there was no defects originated from shrinkage in condensation reaction.

The FT-IR measurement was used to demonstrate the existence of silicon and oxygen atoms in molecular structure of STF. Figure 15 shows the FT-IR spectra of pristine silica after calcined POS at 500℃ in argon for 2h. In the entire samples, the peak at 1020 cm^{-1}~1121 cm^{-1} arises from the Si-O-Si stretching and 950 cm^{-1} arises from Si-OH. The broad band at 3100 cm^{-1}~3400 cm^{-1} in the spectra of the pristine silica is ascribed to O-H vibration peak. The absorption band of C-H at 2972 cm^{-1} and 2920 cm^{-1} and Si-C at 1250 cm^{-1} do

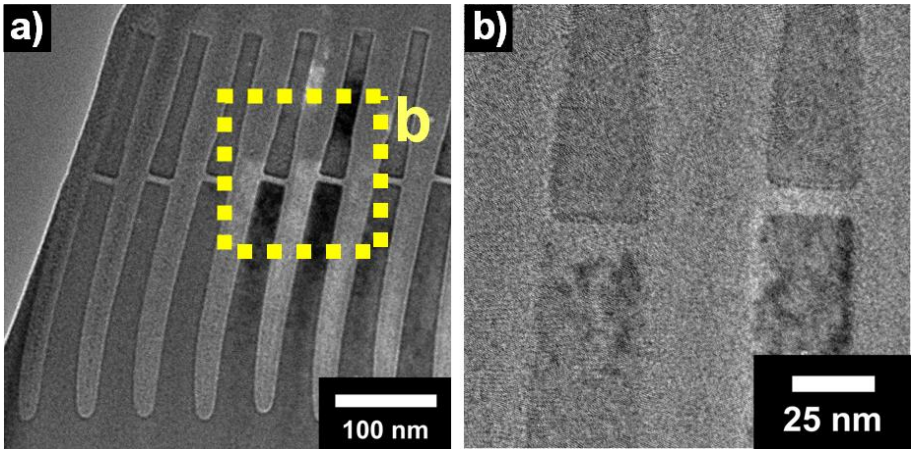

Figure 14. Cross-sectional TEM images of a) the STF filled patterned Si wafer b) the high magnification image of a).

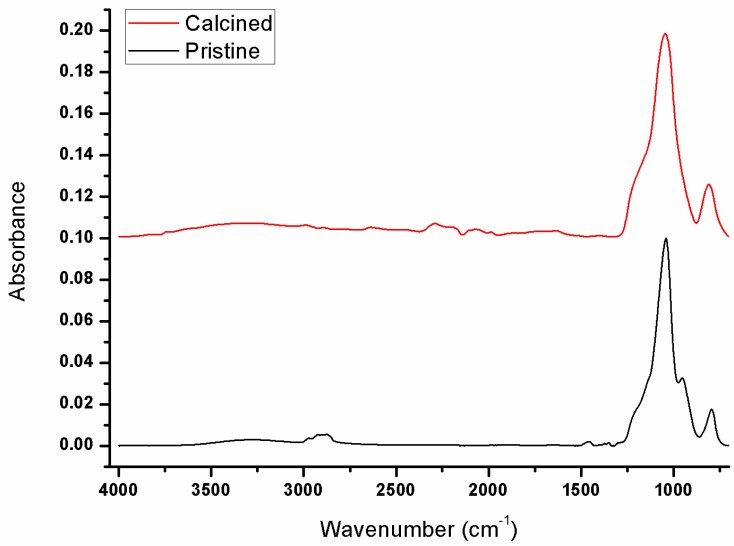

Figure 15. a) FTIR spectra of pristine STF and calcined STF at 500℃ in argon for 2h.

not exist in FT-IR spectra of STF [80]. Therefore, synthesized STF contained silicon and oxygen atoms and there were no carbon atoms after calcinations.

3.1.2. Preparation of Mesoporous Silica in Shallow Trench using Cationic Surfactants and Vaporized Precursor

We report here the VPS of a low-k, crack-free, mesoporous silica film (MSF) in a shallow nanotrench with 25 nm width and 400 nm depth (aspect ratio : 16). TEOS was used as the precursors of the mesoporous silica. Octyltrimethyl-ammonium bromide (OTAB), dodecyltrimethyl-ammonium bromide (DTAB), and cetyltrimethylammonium bromide (CTAB) were selected for the surfactants. Phosphoric acid was used as the catalyst for the condensation reaction that formed the silica in shallow trenchs [81].

The overall procedure for fabrication of MSF in shallow nanotrench is illustrated in Figure 16. The nanopatterned silicon wafer was prepared by argon floride emulsion lithography and 2-step dry etch, and it was used as substrate [82]. Firstly, the wafer was treated with O2 plasma for 1 min with 20 sccm of gas flow rate and 100 W power to provide affinity with aqueous surfactant solution. In case of MSF-16, the plasma treated wafer was soaked into the sufficient amount of surfactant solution composed of CTAB, phosphoric acid and distilled water (weight ratio = 1.37:0.1:9.2) for 5 min. The CTAB was self-assembled on the surface of wafer and the lamellar structured micelles were formed. The cationic heads of CTAB faced to the surface of wafer because of charge-charge interaction between the nitrogen atom of CTAB and hydroxyl

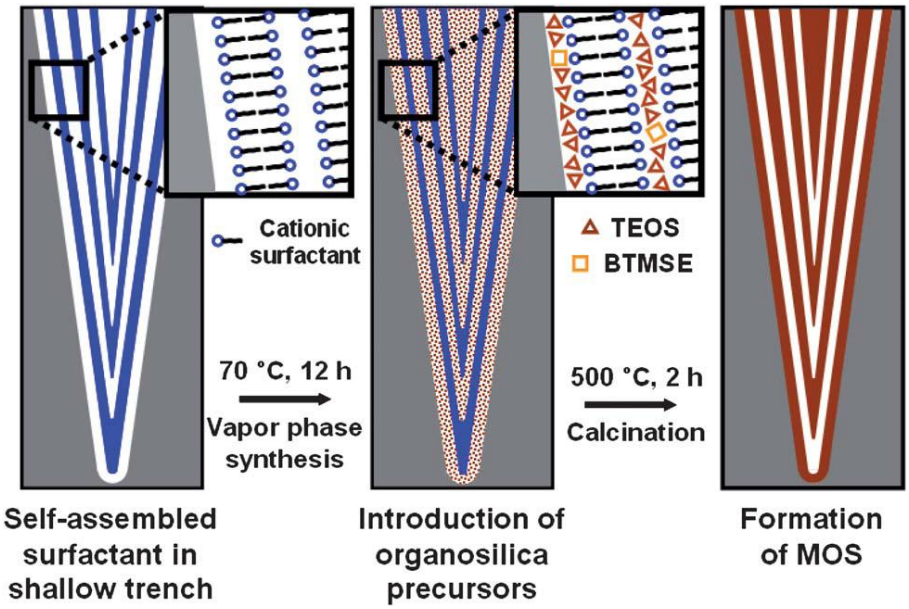

Figure 16. Schematic illustration of the fabrication of mesoporous organosilica using VPS in a shallow trench.

groups of plasma treated wafer. After 5 min soaking, the wafer was taken out from aqueous surfactant solution, and was spun up with 5000 rpm by spin coater for 30 s to remove excess surfactant solution. Then, the wafer was moved into a closed vessel containing vaporized TEOS at 70 ℃ for 30 min. The vaporized reagent was continously diffused into nanogap filled with surfactant micelles. The VPS was performed for 12 h in order to form silica. The wafer that filled with synthesized MSF was obtained by venting the reactor to isolate from residual reagent vapor. The wafer was calcined to produce the molecular structure of MSF-16 and remove CTAB at 500 ℃ in air for 5 h. In addition, MSF-8, MSF-12 were also prepared using surfactant solution containing same amount of OTAB, DTAB as a substitute of CTAB, repectively.

Figure 17 displays field-emission scanning electron microscope (FE-SEM) images of surface and a section of the pristine wafer and the MSF coated wafer. The FE-SEM images clearly show that the trenches of the pristine wafer were covered with synthesized silica. In figure 17a, the wafer has vertically aligned shallow trenches and the width and feature size of them were 25 nm and 25 nm, respectively. There were no significant defects at trenches what were originated from pre-treatment such as cutting, plasma treatment, and washing. Figure 17b shows surface of the wafer after reaction. The nanopattern was fully covered with MSF and trenches were could not be observed with

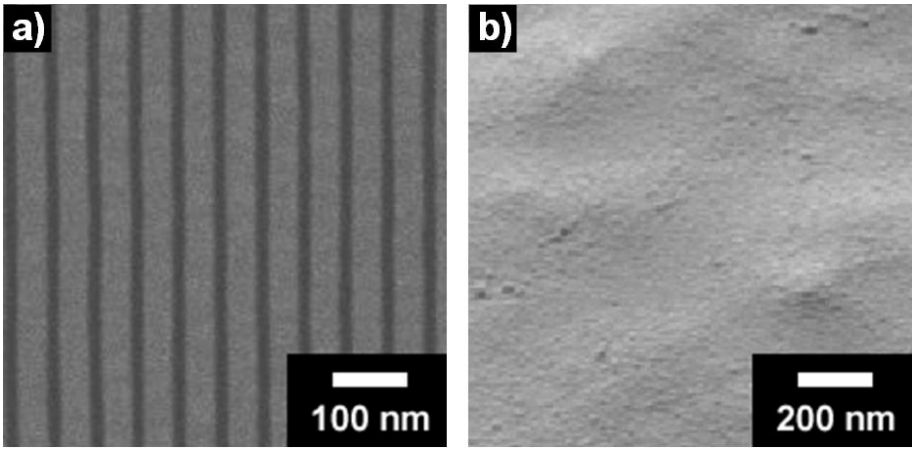

Figure 17. Surfacial FE-SEM images of a) the pristine wafer b) MSF filled patterned Si wafer.

perpendicular viewpoint. MSF had smooth surface and there was no significant defects such as crack and distortion.

Figure 18 displays cross-sectional field-emission scanning electron microscope (FE-SEM) images of the MSF-filled wafer. The FE-SEM images clearly show the vertical reverse- triangular-shaped trenches, which had 25 nm width and 400 nm depth with a feature size of 25 nm. For Figure 18b, a focused ion beam (FIB) was used to image the cross-section of the MSF-filled wafer; a back-scattered electron (BSE) detector was used to distinguish silicon from the MSF [82]. The synthesized MSF indicates darker than the crystalline silicon of the wafer in the BSE detector because silicon is heavier than the carbon and oxygen atoms in the MSF. Dark regions in middle of Si wafer represented silica layer that originated from 2-step dry etch in the wafer preparation. To the best of our knowledge, there are no reports that representing the fabrication of mesoporous silica in shallow trench with dimensions less than 50 nm [83-86]. Under our experimental condition, the trenches and walls with 25 nm width did not collapse without significant shrinkage during condensation reaction.

To evaluate the mesoporous structure of the MSF-16, a cross sectional TEM image was obtained using FIB. The trench after VPS is illustrated in Fig. 19a. The CTAB surfactant enabled the formation of a lamellar structure on the

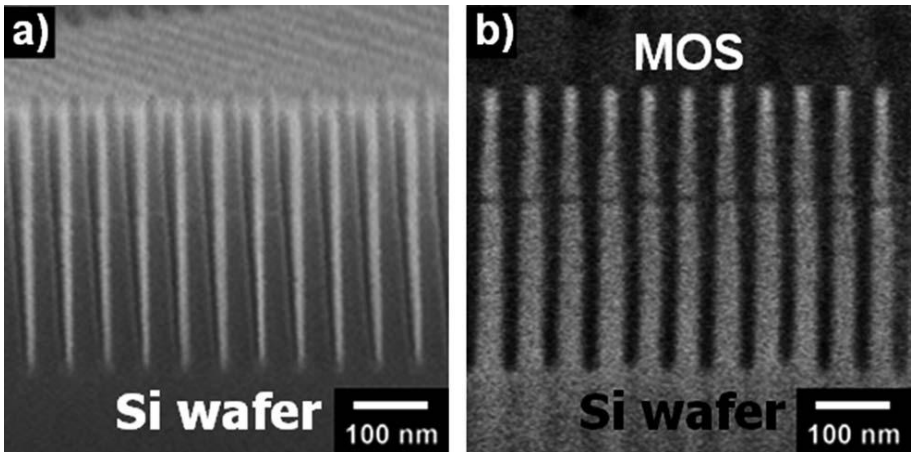

Figure 18. Cross-sectional FE-SEM images of the (a) patterned Si wafer and (b) MSF filled patterned Si wafer.

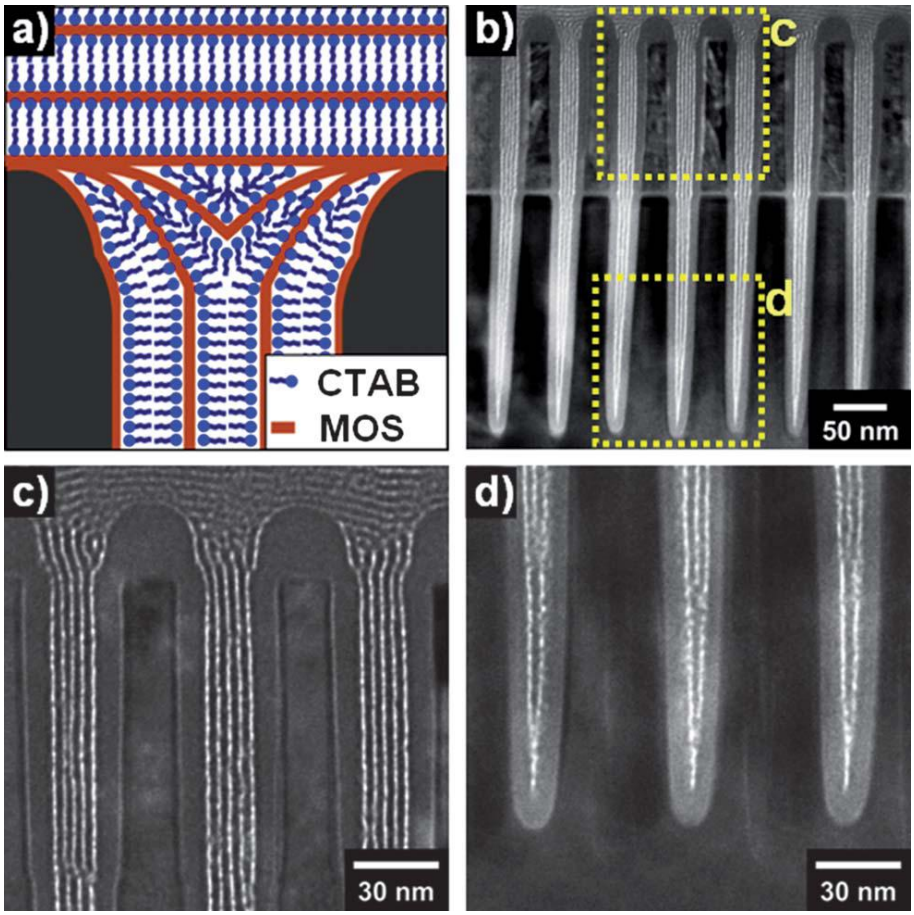

Figure 19. (a) Schematic illustration of the mesostructure of the organosilica layer that was structured by self-assembled CTAB. (b) Overall crosssectional TEM images of patterned Si wafer filled with MOS, (c) and (d) higher magnification of the boxed areas in (b).

surface of the silicon wafer.6 MSF-16 was formed between the heads of CTAB molecules in the CTAB layers due to charge–charge interactions [87-89]. This mesostructure was anticipated to have a closed pore after CMP. Fig. 19b shows the MSF filled trenches. The morphology of MSF was uniform from the wide top to the narrow bottom of the trenches. It indicated that the vaporized precursors could penetrate into the surfactant solution and the MSF was formed via a condensation reaction [90]. High-magnification TEM images (Fig. 19c and d) demonstrated that the well ordered lamellar structures of the MSF in the trenches was crack free. In Fig. 19c, the mesostructure of the MSF was parallel to the wall of the wafer and had four layers. The distance between each layer of the MSF was approximately 4 nm in TEM observation, which agreed well with the d-spacing data in Table 1 from small angle X-ray diffraction (SAXS). The number of folds decreased to one at the bottom of the shallow trench because of the narrow space (Fig. 19d) [91]. No significant cracking or leaning occurred from the top to the bottom of trenches. The plasma treatment provided hydroxyl groups on the surface of the silicon wafers, and these functional groups formed chemical bonds with the silica precursors. Based on these data, a defect-free MSF with ultra-high-aspect-ratio trenches could be produced by VPS.

Fig. 20 represents the cross-sectional images of MSFs which were synthesized using DTAB and OTAB surfactants as structure-directing agents. Compared with CTAB, DTAB could also form a mesoporous structure in a shallow trench (Fig. 20a).MSF-12 filled the trenches and did not possess significant defects such as cracking or voids. In Fig. 20c, MSF-12 contained a dual mesoporous system: MSF on the surface of pattern had a hexagonal structure, and MSF in the trench had a lamellar structure. This meant that hexagonal MSF on the surface could protect MSF in the trench from defects and pollutants while CMP [92]. On the other hand, as shown in Fig. 20b, OTAB could not create a well-ordered mesoporous structure under our experimental conditions. The shallow trench was filled with disordered MSF and barely closed. OTAB is less hydrophobic than DTAB and CTAB because of its short alkyl chain spacer [93-95]. Therefore, the driving force for construction of a micelle structure was insufficient to form an ordered mesoporous structure (Fig. 20d) [93]. We conclude from these results that the chain length of cationic surfactants was important to form a mesoporous structure.

Fig. 21 shows the nitrogen adsorption/desorption isotherms of the synthesized MSF-16. For nitrogen adsorption/desorption isotherms measurement, MSF powder samples using CTAB, DTAB, and OTAB were

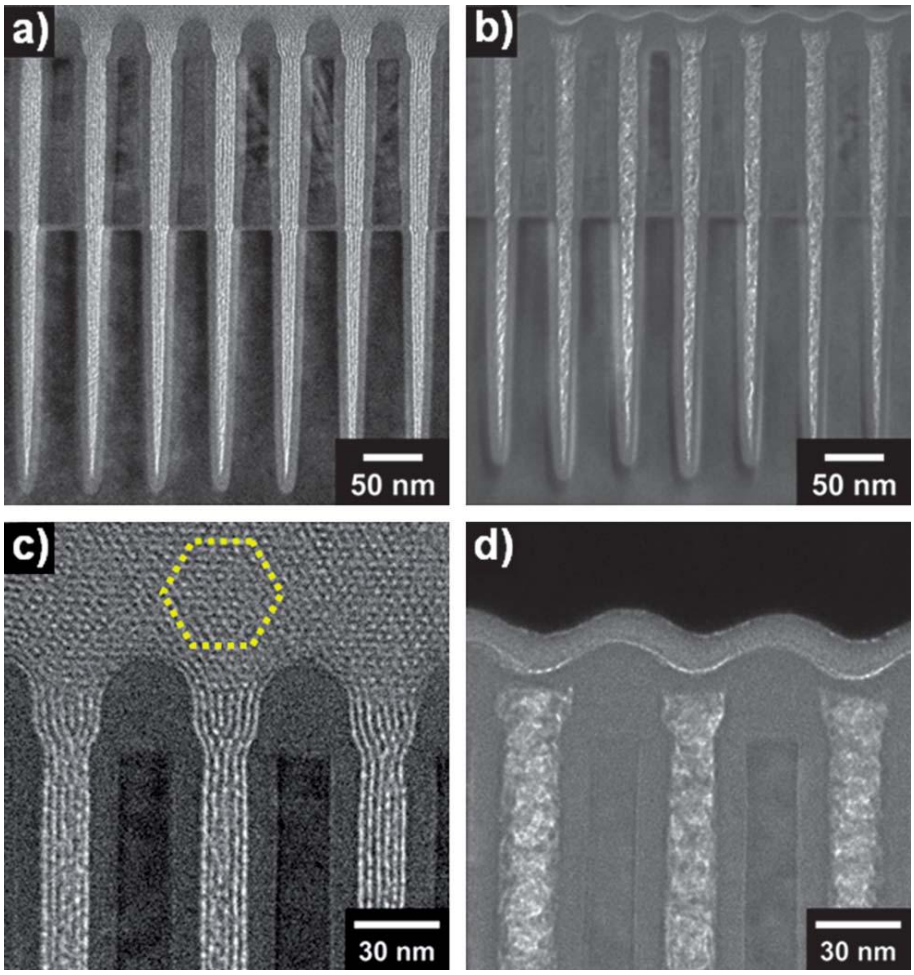

Figure 20. Overall cross-sectional TEM images of the Si wafer filled with MOS that was structured by (a) DTAB and (b) OTAB. (c and d) Higher magnification of (a) and (b), respectively.

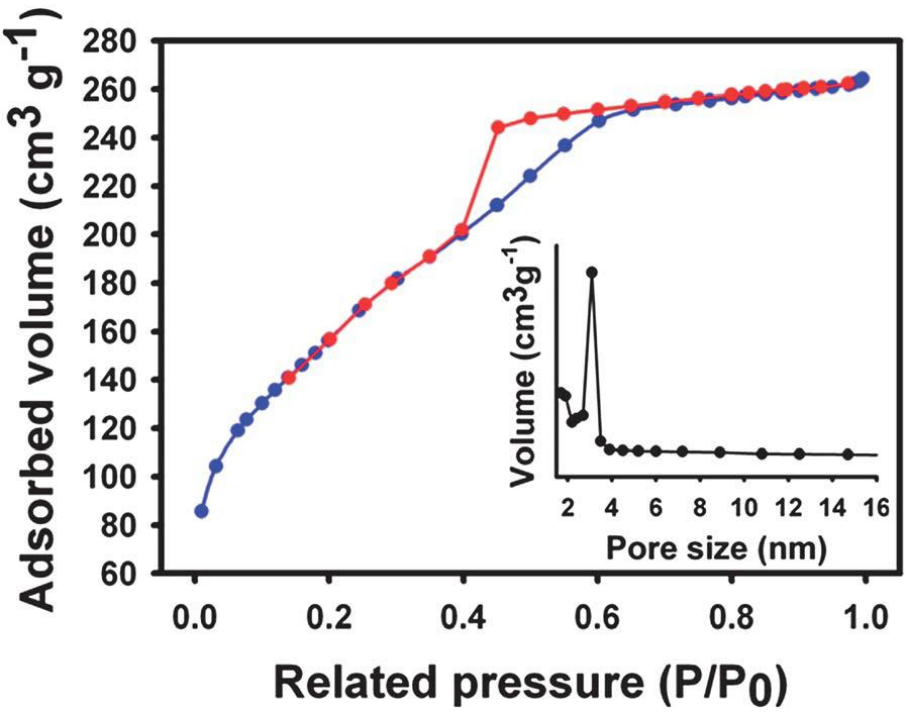

Figure 21. Nitrogen adsorption/desorption isotherms of MOS (inset: pore size distribution obtained by BJH adsorption branches of MOS).

fabricated and collected at the surface of pristine wafers without patterns under the same experimental conditions of the patterned wafer. Approximately 0.1 g of the sample was used for nitrogen adsorption/desorption isotherms measurement. The obtained isotherms had a type IV hysteresis loop according to the Brunauer classification scheme [96]. The inset of Fig. 21 shows the graph of pore-size distribution (PSD) as calculated by the Barrett, Joyner, and Halenda (BJH) method. The Brunauer–Emmett–Teller (BET) surface area of MSF was calculated to be 589.74m^2 g^{-1}, and the average pore size value of the MSF was estimated to be 3.04 nm (Table 2). The hysteresis loop and PSD plot indicated that the MSF had open pores. The SAXS pattern for the MSF clearly showed a 100 reflection at 1.00 (2ɵ degrees) and a d-spacing value of 3.97 nm.

The SAXS patterns were deconvoluted to obtain the degree with maximum intensity at Figure 22. The 2θ degree values of MSF-8, MSF-12, MSF-16 were 2.85, 2.59, 2.27, respectively. These values were used to calculate the d-spacing of each samples using Bragg equation [97].

The FT-IR measurement was used to demonstrate the existence of silicon and oxygen atoms in molecular structure of STF. Figure 23 shows the FT-IR spectra of pristine silica after calcined POS at 500℃ in argon for 2h. In the entire samples, the peak at 1020 cm^{-1}~1121 cm^{-1} arises from the Si-O-Si stretching and 950 cm^{-1} arises from Si-OH. The broad band at 3100 cm^{-1}

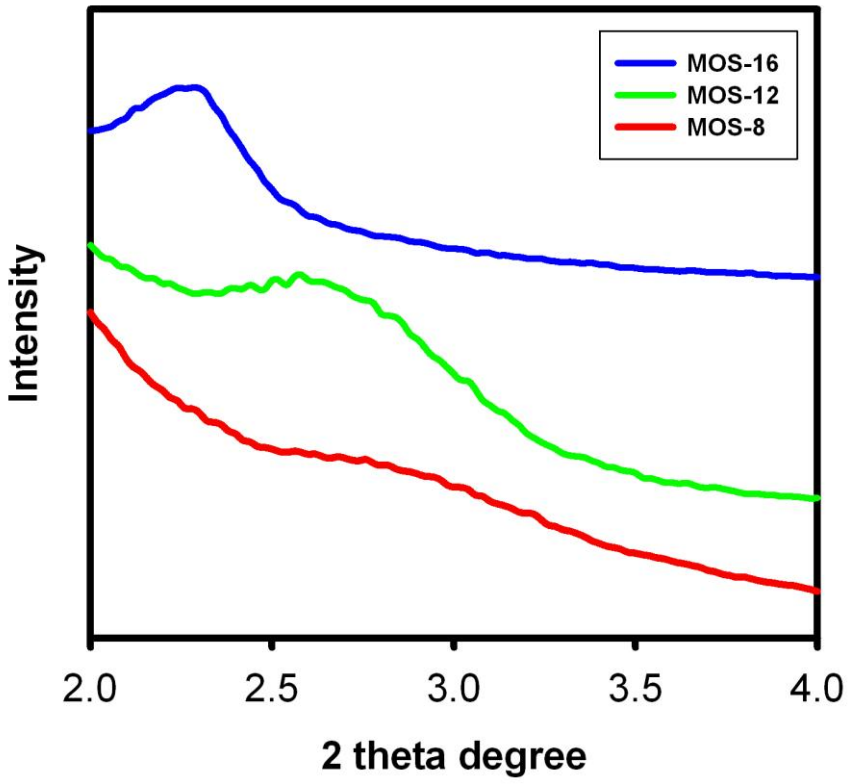

Figure 22. XRD patterns of MSF series.

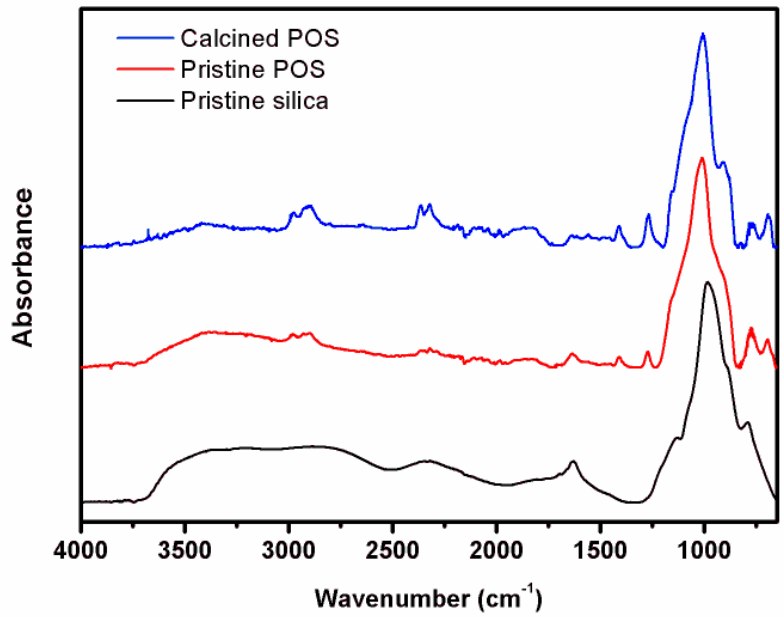

Figure 23. FTIR spectra of pristine silica, pristine STF and calcined STF at 500℃ in air for 2h.

3400 cm^{-1} in the spectra of the pristine silica is ascribed to O-H vibration peak. The absorption band of C-H at 2972 cm-1 and 2920 cm^{-1} and Si-C at 1250 cm^{-1} do not exist in FT-IR spectra of STF [97]. Therefore, synthesized STF contained silicon and oxygen atoms and there were no carbon atoms after calcinations.

The physical properties of various MSF are summarized in Table 2. Their dielectric constants were also calculated from the dielectric constant of dense silica (ca. 4.0) and the porosity of the MSF as measured by the nitrogen adsorption/desorption isotherm [98, 99]. As shown in Table 2, as the tail spacer length of the surfactant increased from 8 to 16, the calculated dielectric constant decreased from 1.84 to 1.73. According to the d-spacings and the average pore sizes, the wall thicknesses of the MSFs were similar (ca. 1 nm). The MSF synthesized in CTAB had the largest void fraction in the mesoporous structure, and it had the lowest dielectric constant. Its calculated dielectric constant (1.73) is low enough for the filling of nanotrenches below 20 nm wide. The elastic modulus of MSFs was measured by an atomic force microscopy (AFM) nanoindentation technique [100, 101]. The results were 6.14, 6.61, and 6.84 N m^{-2}, respectively, for MSF-8, MSF-12, and MSF-16. The highest value is approximately 1.5 times that of conventional materials such as pure mesoporous silica (ca. 4.0Nm^{-2}). The low value for MSF-8 was responsible for

Table 2. Physical properties of MOSs depending on the chain length of cationic surfactants.

Samples	Surfactant	Alkyl chain length	D spacing [a]	Average pore size [b]	BET surface area	Porosity	Dielectric constant of MOS	Young's modulus
		[Å]	[nm]	[nm]	[m^3g^{-1}]	[%]	[ε]	[Nm^{-2}]
Organosilca (control)	-	-	-	-	-	-	3.93	9.00
MOS-8	OTAB	9.2	3.10	2.09	616.31	53.2	1.84	6.14
MOS-12	DTAB	13.8	3.41	2.54	687.85	55.1	1.76	6.61
MOS-16	CTAB	18.4	3.97	3.04	589.74	55.9	1.73	6.84

the deformation of the mesoporous structure. Nevertheless, it meets the minimum stiffness requirement (<6 N m^{-2}) for nanogapfilling materials.

3.1.3. Synthesis of highly porous silica in shallow trench for low-k application

We report here the synthesis of a highly porous silica (HPS) using two surfactants, cetyltrimethylammonium bromide (CTAB) and Pluronic F127, as structure-directing agents. These surfactants were self-assembled and built the micelle structure in surfactants solution [102]. After micelle formation, vaporized reactants were penetrated into surfactants solution and gathered at the surface of micelle. The ordered clusters of reactants by micelles were condensed to silica by catalyst. After condensation and calcinations, surfactants were removed and formed voids, thereby provided a low dielectric constant to HPS.

The overall synthesis of the HPS in shallow trenches of a patterned wafer is illustrated in Figure 24. First, the patterned wafer was exposed to O2 plasma (100 W, 30 s). The oxygen plasma treated wafer surface was hydrophilic and had a negative charge due to newly formed hydroxyl functional groups [10]. After plasma treatment, the wafer was immersed in a dual-surfactant solution containing a cationic and a nonionic surfactant. The surface hydroxyl groups of the shallow trenches interacted with the positively-charged heads of the cationic surfactants and the hydrophilic polyethyleneoxide (PEO) segments of the nonionic surfactant [103]. After micelle formation, the wafer was spin

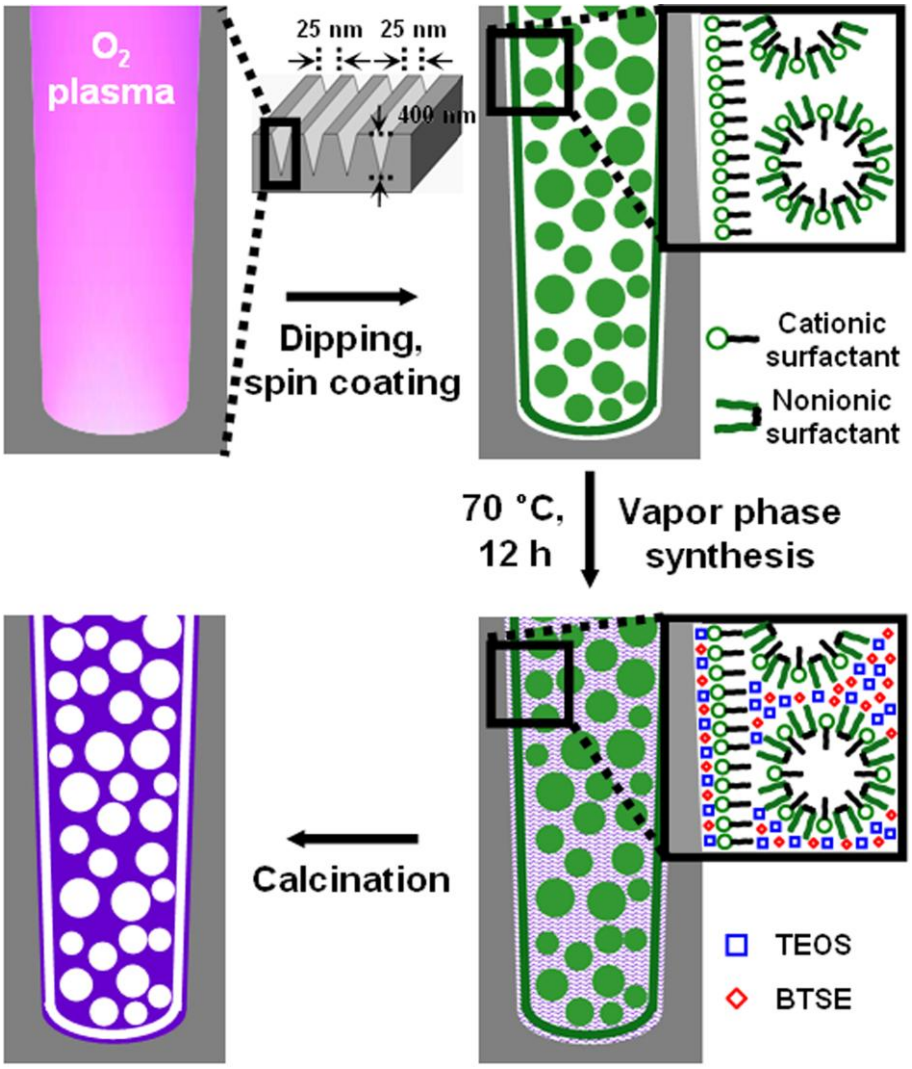

Figure 24. Schematic illustration of the synthesis of POS by VPS in shallow trench

coated at 5000 rpm for 30 s to remove excess surfactant solution. The wafer was placed in the closed vessel containing vaporized precursors. The precursors were hydrolyzed to silanol during exposure to the surfactant solution at 70 ℃ for 12 h [104]. Subsequent treatment with phosphoric acid condensed the precursors into the porous silica. The wafer was finally calcined in a furnace at 500 ℃ for 2 h to remove excess water and surfactants.

Figure 25 displays field-emission scanning electron microscope (FE-SEM) images of surface of the pristine and HPS coated wafer. The FE-SEM images clearly show that the trenches of the pristine wafer were covered with synthesized silica. In figure 25a, the wafer has vertically aligned shallow trenches and the width and feature size of them were 25 nm and 25 nm, respectively. There were no significant defects at trenches what were originated from pre-treatment such as cutting, plasma treatment, and washing. Figure 25b shows surface of the wafer after reaction. The nanopattern was fully covered with HPS and trenches were could not be observed with perpendicular viewpoint. HPS had smooth surface and there was no significant defects such as crack and distortion.

Figure 26 shows cross-sectional field-emission scanning electron microscopy (FE-SEM) images of pristine and HPS-filled wafers. The pristine wafer had thin walls and reverse-triangle-shaped trenches (Figures 26a and

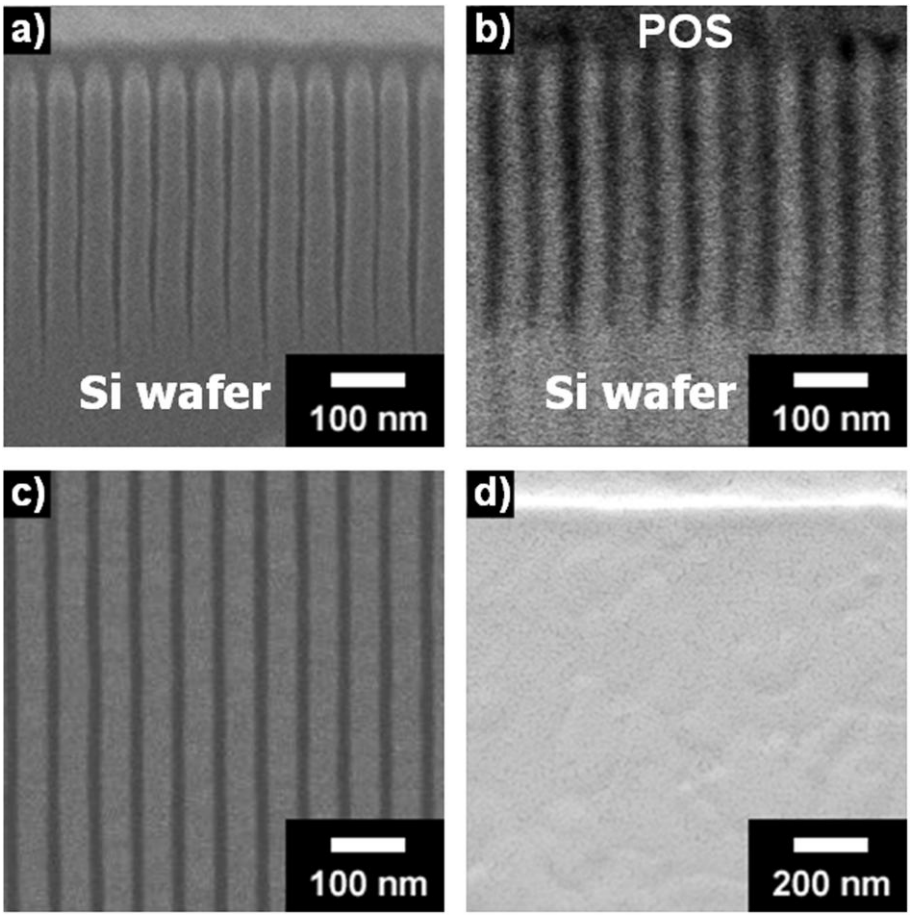

Figure 25. Cross-sectional FE-SEM images of a) patterned Si wafer, b) POS filled patterned Si wafer. Surface FE-SEM images of c) patterned Si wafer, d) POS filled Si wafer.

26c) with a width, depth, and feature size of 25 nm, 400 nm, and 25 nm, respectively. Cross-sectional images of the HPS-filled wafer are given in Figures 25b and 25d. Focused ion beam (FIB) and back-scattered electron (BSE) detection were used to obtain the image of Figure 26b. These methods could distinguish the pure silicon wafer from the synthesized silica film on flat, vertical sections. With the BSE detector, heavier atoms appear brighter than lighter atoms [106]. The HPS appears darker than the silicon wafer because it contains atoms that are lighter than silicon, i.e., carbon and oxygen. Therefore, in figure 26b, HPS (darker region) filled trenches of the wafer without voids or crack. Figure 26d shows the surface of the patterned wafer after synthesis of the HPS. The surface was flat without significant roughness and defects. This meant that the surface of spin coated solution was flat, and the smooth surface remained after vapor phase synthesis (VPS). It was therefore expected that HPS could fill shallow trenches without significant cracking or tilting.

The mesoporous structure of the HPS was investigated using ultramicrotomed samples prepared by FIB. Transmission electron microscopy (TEM) images (Figure 27) show that the HPS on the patterned wafer had a highly porous and defect-free structure. The CTAB and F127 molecules in the mixed surfactant solution assembled and occupied space in the trenches [107]. Voids formed when the surfactants decomposed. Homogeneous distribution of

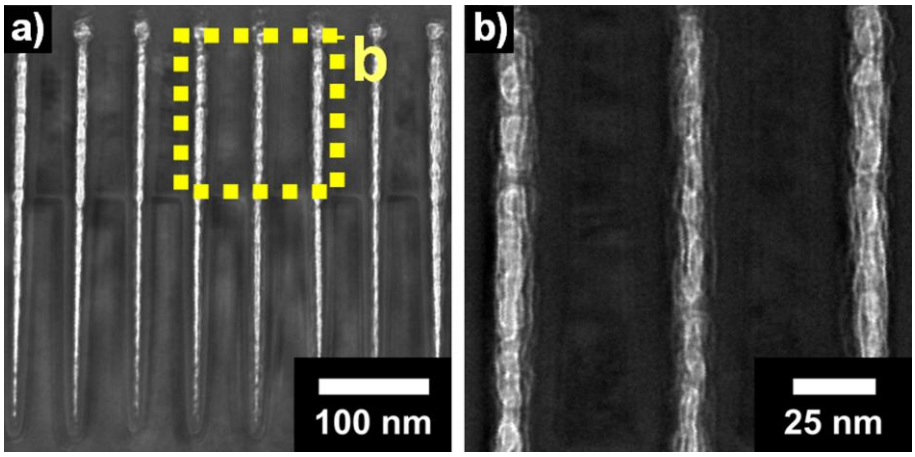

Figure 27. a) Overall cross-sectional TEM images of patterned Si wafer filled with POS, b) higher magnification of the boxed area in a).

phosphoric acid catalyst in the trenches with continuous feeding of vaporized TEOS and BTE during the condensation reaction led to uniform filling of the trenches by the HPS. High-magnification images (Figure 27b) reveal the detailed structure of the HPS in the trenches. Silica layers were formed between the walls, and created pores. The HPS contained more air voids (k = 1) than a conventional mesoporous silica and thus had a lower dielectric constant [108]. Internal voids could be protected from dirt by dense silica on the tops of the trenches [97]. These results indicated that the HPS was suitable for defect-free filling of trenches.

Fig. 28 shows the nitrogen adsorption/desorption isotherms of the synthesized MSF-16. For nitrogen adsorption/desorption isotherms measurement, MSF powder samples using CTAB, DTAB, and OTAB were fabricated and collected at the surface of pristine wafers without patterns under the same experimental conditions of the patterned wafer. Approximately 0.1 g of the sample was used for nitrogen adsorption/desorption isotherms measurement. The obtained isotherms had a type IV hysteresis loop according to the Brunauer classification scheme [87]. The inset of Fig. 28 shows the graph of pore-size distribution (PSD) as calculated by the Barrett, Joyner, and Halenda (BJH) method. The Brunauer–Emmett–Teller (BET) surface area of MSF was calculated to be 589.74m2 g 1, and the average pore size value of

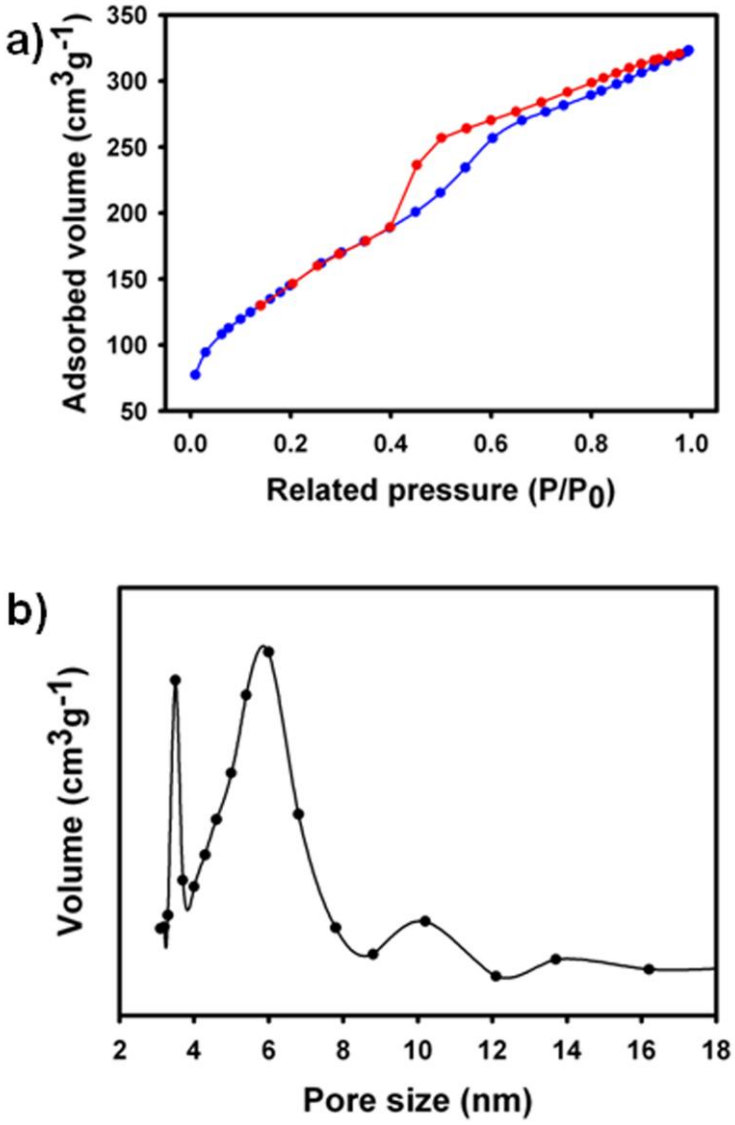

Figure 28. a) Nitrogen adsorption/desorption isotherms of MSF. b) Pore size distribution of MSF.

the MSF was estimated to be 3.04 nm (Table 3). The hysteresis loop and PSD plot indicated that the MSF had open pores.

The FT-IR measurement was used to demonstrate the existence of silicon and oxygen atoms in molecular structure of STF. Figure 29 shows the FT-IR spectra of pristine silica after calcined POS at 500℃ in argon for 2h. In the entire samples, the peak at 1020 cm^{-1}~1121 cm^{-1} arises from the Si-O-Si stretching and 950 cm^{-1} arises from Si-OH. The broad band at 3100 cm^{-1}~3400 cm^{-1} in the spectra of the pristine silica is ascribed to O-H vibration peak. The absorption band of C-H at 2972 cm^{-1} and 2920 cm^{-1} and Si-C at 1250 cm^{-1} do not exist in FT-IR spectra of STF. Therefore, synthesized STF contained silicon and oxygen atoms and there were no carbon atoms after calcinations.

Physical properties of the POS are summarized in Table 3. The dielectric constant was calculated from the porosity obtained by BET measurements and the dielectric constant of dense silica (ca. 4) prepared by the sol-gel method [76]. The calculated value of 1.57 satisfies the minimum requirement for filling trenches narrower than 15 nm [92]. The c-v measurements using MIS structure were employed to measure the capacitance of POS and the data was used to calculate actual dielectric constant. The actual dielectric constant was 1.65 and higher than the calculated value. The discrepancy between ideally calculated value and actual value might be originated from adsorbed water molecules.

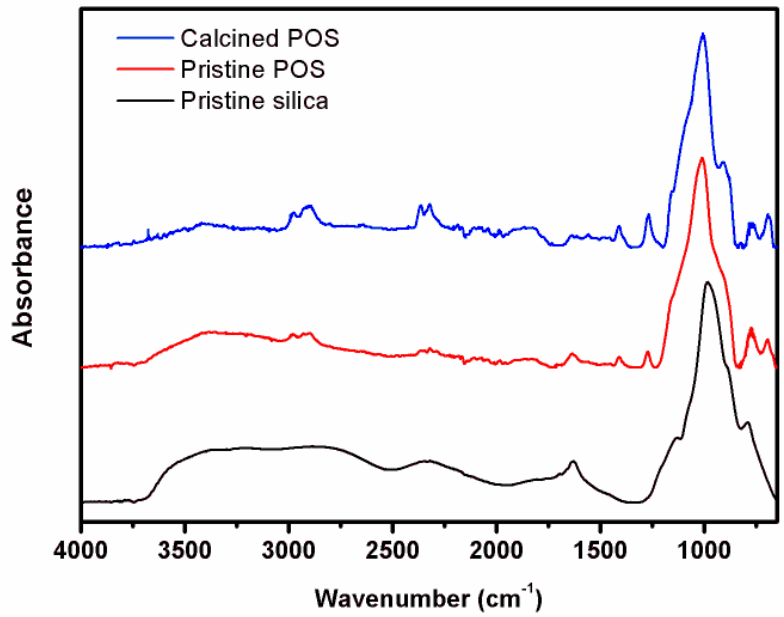

Figure 29. FTIR spectra of pristine silica, pristine STF and calcined STF at 500℃ in air for 2h.

Table 3. Physical properties of pristine organosilica and POS

	Average pore size [a]	BET surface area	Porosity	Dielectric constant of POS	Young's modulus
	[nm]	[m^2g^{-1}]	[%]	[ε]	[Nm^{-2}]
Pristine organosilica	-	-	-	3.65	9.00
POS	4.67	506.56	56.9	1.57	5.20

[a] The average value of PSD plot by BJH method.

Water molecules easily adsorbed on the silica and rose up the dielectric constant. An atomic force microscopy nanoindentation technique was used to measure the elastic modulus [52, 68]. The Young's modulus was ca. 5.20 GPa, suitable for gap-filling.

3.2. Fabrication of Modified Mesoporous Silica with Enhanced Physical Properties for Low-k applications

3.2.1. Elastic Modulus Modification of Mesoporous Silica Using Crosslinking Agent

We report here the VPS of a low-k, crack-free, mesoporous organosilica (MOS) in a shallow nanotrench with 25 nm width and 400 nm depth (aspect ratio : 16). TEOS and BTE were used as the precursors of the mesoporous silica. BTE created crosslinked molecular structure at synthesized MOS, and reinforeced the physical properties including elastic modulus, dielectric constant. Cetyltrimethylammonium bromide (CTAB) was selected for the surfactant. Phosphoric acid was used as the catalyst for the condensation reaction that formed the silica in shallow trenchs.

The overall procedure for fabrication of MOS in shallow nanotrench is illustrated in Figure 30. The nanopatterned silicon wafer was prepared by argon floride emulsion lithography and 2-step dry etch, and it was used as substrate [71]. Firstly, the wafer was treated with O2 plasma for 1 min with 20 sccm of gas flow rate and 100 W power to provide affinity with aqueous surfactant solution. The plasma treated wafer was soaked into the sufficient amount of surfactant solution composed of CTAB, phosphoric acid and distilled water (weight ratio = 1.37:0.1:9.2) for 5 min. The CTAB was self-assembled on the

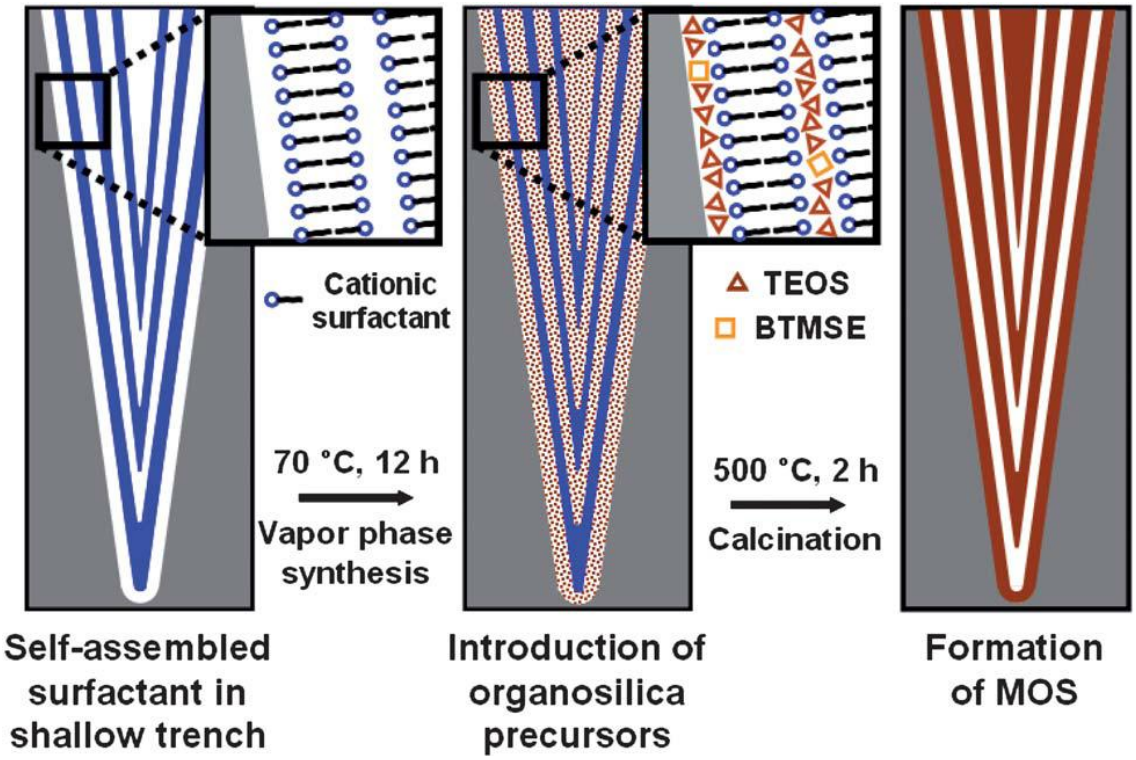

Figure 30. Schematic illustration of the fabrication of mesoporous organosilica using VPS in a shallow trench.

surface of wafer and the lamellar structured micelles were formed. The cationic heads of CTAB faced to the surface of wafer because of charge-charge interaction between the nitrogen atom of CTAB and hydroxyl groups of plasma treated wafer. After 5 min soaking, the wafer was taken out from aqueous surfactant solution, and was spun up with 5000 rpm by spin coater for 30 s to remove excess surfactant solution. Then, the wafer was moved into a closed vessel containing vaporized TEOS and BTE at 70 ℃ for 30 min. The vaporized reagents were continuously diffused into nanogap filled with surfactant micelles. The VPS was performed for 12 h in order to form organosilica. The wafer that filled with synthesized MOS was obtained by venting the reactor to isolate from residual reagent vapor. The wafer was calcined to produce the molecular structure of MOS and to remove CTAB at 500 ℃ in argon for 2 h.

Figure 31 displays field-emission scanning electron microscope (FE-SEM) images of surface and a section of the pristine wafer and the MOS coated wafer. The FE-SEM images clearly show that the trenches of the pristine wafer were covered with synthesized silica. In figure 31a, the wafer has vertically aligned shallow trenches and the width and feature size of them were 25 nm and 25 nm, respectively. There were no significant defects at trenches what were originated from pre-treatment such as cutting, plasma

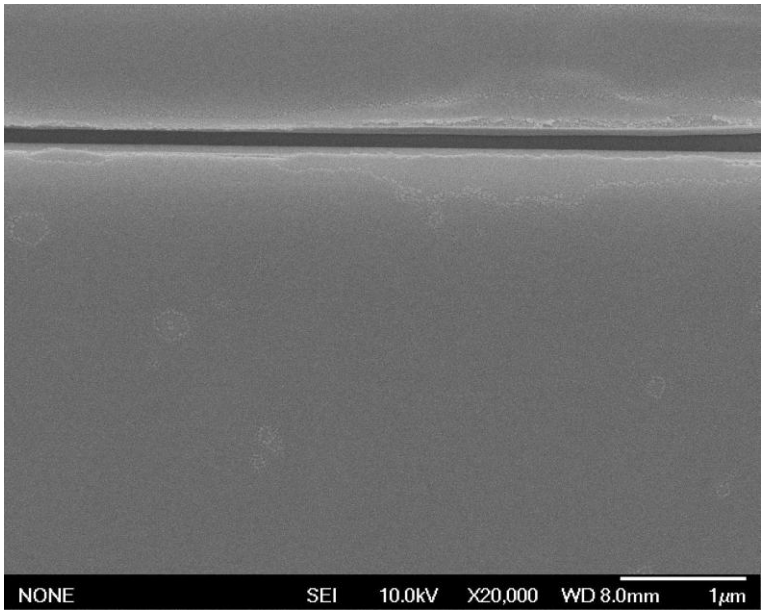

Figure 31. Surfacial FE-SEM images of the MOS filled patterned Si wafer.

treatment, and washing. Figure 31b shows surface of the wafer after reaction. The nanopattern was fully covered with MOS and trenches were could not be observed with perpendicular viewpoint. MOS had smooth surface and there was no significant defects such as crack and distortion.

Figure 32 displays cross-sectional field-emission scanning electron microscope (FE-SEM) images of the MOS-filled wafer. The FE-SEM images clearly show the vertical reverse- triangular-shaped trenches, which had 25 nm width and 400 nm depth with a feature size of 25 nm. For Figure 32b, a focused ion beam (FIB) was used to image the cross-section of the MOS-filled wafer; a back-scattered electron (BSE) detector was used to distinguish silicon from the MOS. The synthesized MOS indicates darker than the crystalline silicon of the wafer in the BSE detector because silicon is heavier than the carbon and oxygen atoms in the MOS [72]. Dark regions in middle of Si wafer represented silica layer that originated from 2-step dry etch in the wafer preparation. To the best of our knowledge, there are no reports that representing the fabrication of mesoporous silica in shallow trench with dimensions less than 50 nm. Under our experimental condition, the trenches and walls with 25 nm width did not collapse without significant shrinkage during condensation reaction.

Figure 33 represents the TEM images of mesoporous silica which

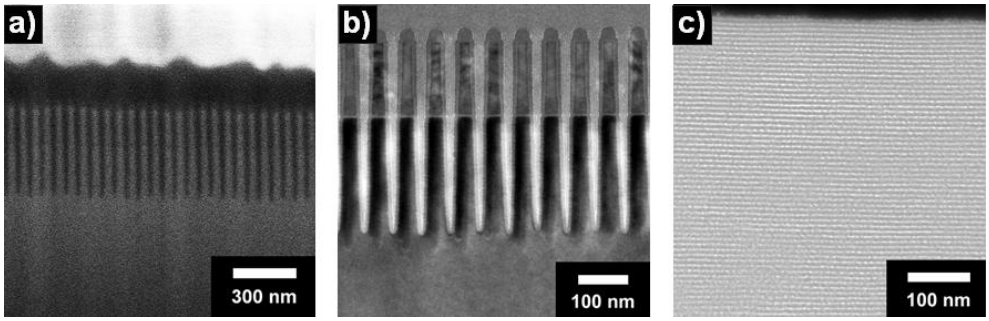

Figure 32. Cross-sectional FE-SEM images of the MOS filled patterned Si wafer.

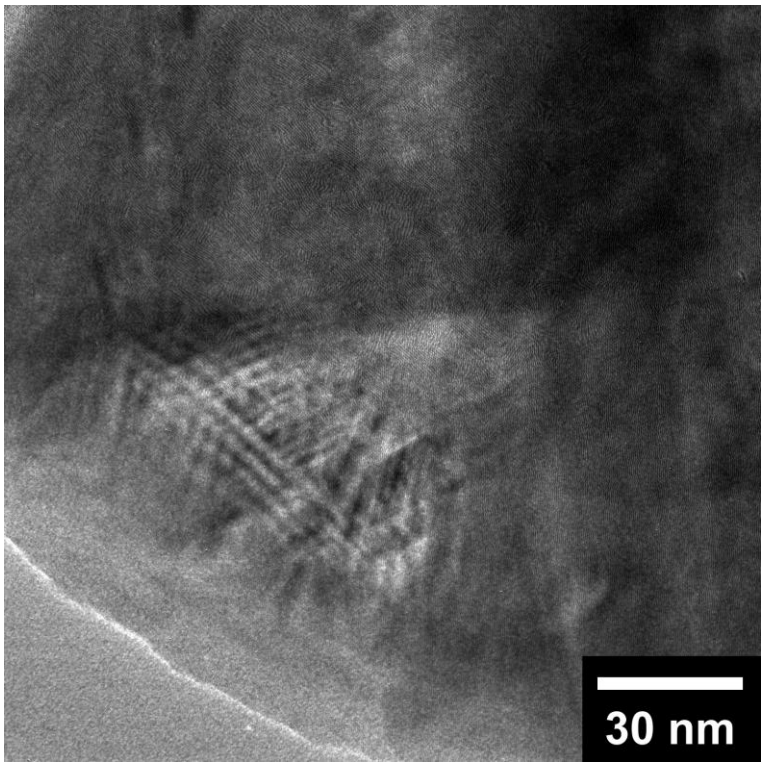

Figure 33. TEM image of powder sample of fabricated MOS which gathered from surface of Si wafer.

synthesized using vaporized TEOS and BTE as precursors. Compared with mesoporous silica by pure TEOS, significant difference was not observed. The CTAB enabled the formation of well ordered lamellar mesoporous structure for MOS. This meant that vaporized TEOS and BTE showed similar behavior in vapor phase and hydrolyzed state. The pore size of the MOS was approximately 3 nm in TEM observation, which agreed well with the pore size data in Table 1 from BET measurement. And this data well matched with the general pore size of mesoporous silica by CTAB as surfactant. Judging from these data, vapor phase synthesis could be applied to fabricated functionalized organosilica with mesoporous structure.

Figure 34 represents the reaction mechanisms of TEOS (Figure 34a) and BTE (Figure 34b) by acidic condition, water and catalyst at 70 ℃. These mechanisms were suitable at ideal reaction condition with pure precursors. The FT-IR measurement was used to demonstrate the existence of carbon atoms in molecular structure of MOS after calcinations. Table 4 shows the chemical composition of MOS compared with silica gel and pristine organosilica. The EDS analyze was employed to measure the weight ratio, and atomic ratio of samples were calculated from the weight ratio and molecular weight. Pure silica gel did not contain carbon elements and atomic ratio of O/Si was 1.95. Also, atomic ratio of O/Si of sol-gel synthesized pristine organosilica and MOS

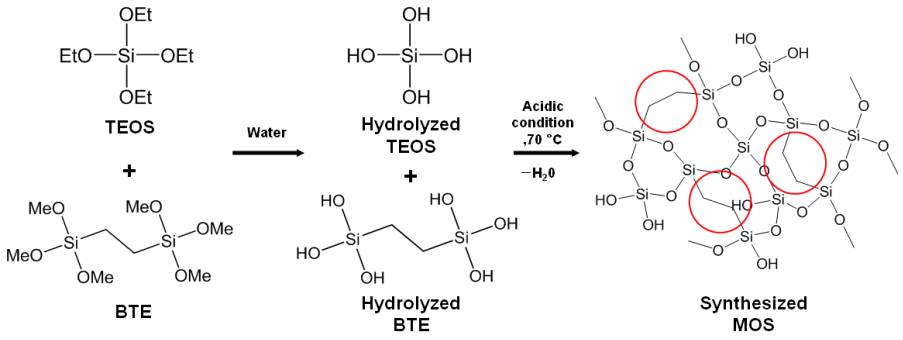

Figure 34. Schematic illustration of the reaction mechanism of organosilica by TEOS and BTE

were 1.93 and 1.95, respectively. These atomic value were lower than the theoretical value of silica (O/Si = 2). This may be originated from imperfect molecular structure of samples [19, 20]. The pristine organosilica and MOS contained carbon atoms in those molecular structures. The theoretical atomic ratio of C/Si was 0.61 which was similar with that of pristine organosilica. However, the atomic ratio of C/Si of MOS was 0.55, and it was slightly lower than the theoretical value. This low carbon content of MOS was resulted from different molecular weight of BTE (M.W = 270.43) and TEOS (M.W = 208.33). BTE is heavier than TEOS, and it make BTE hard to evaporate. Therefore, the supply speed of BTE was slower than TEOS to surface of surfactants solution. It induced lower content of BTE in synthesized MOS than sol-gel synthesized organosilica.

Table 4. Chemical compositions of silica gel, pristine organosilica (50 wt% BTSE) and POS.[a]

	Atomic ratio (%)			O/Si	C/Si
	C	Si	O		
Silica gel	-	33.92	66.08	1.95	-
Pristine organosilica	17.13	28.46	54.41	1.93	0.60
POS	15.5	28.63	55.87	1.95	0.54

[a] The atomic ratio were calculated from weight ratio of each samples.

Fig. 35 shows the nitrogen adsorption/desorption isotherms of the synthesized MOSs. For nitrogen adsorption/desorption isotherms measurement, MOS powder samples using CTAB and different BTE ratio were fabricated and collected at the surface of pristine wafers without patterns under the same experimental conditions of the patterned wafer. Approximately 0.1 g of the sample was used for nitrogen adsorption/desorption isotherms measurement. The obtained isotherms had a type IV hysteresis loop according to the Brunauer classification scheme. The inset of Fig. 35 shows the graph of pore-size distribution (PSD) as calculated by the Barrett, Joyner, and Halenda (BJH) method. The Brunauer–Emmett–Teller (BET) surface area of MOS was calculated to be 589.74m2 g^{-1}, and the average pore size value of the MOS was estimated to be 3.04 nm (Table 5). The hysteresis loop and PSD plot indicated that the MOS had open pores.

The physical properties of various MOS are summarized in Table 5. Their dielectric constants were also calculated from the dielectric constant of dense silica (ca. 4.0) and the porosity of the MOS as measured by the nitrogen adsorption/desorption isotherm. As shown in Table 1, as the tail spacer length of the surfactant increased from 8 to 16, the calculated dielectric constant decreased from 1.84 to 1.73. According to the d-spacings and the average pore sizes, the wall thicknesses of the MOSs were similar (ca. 1 nm). The MOS

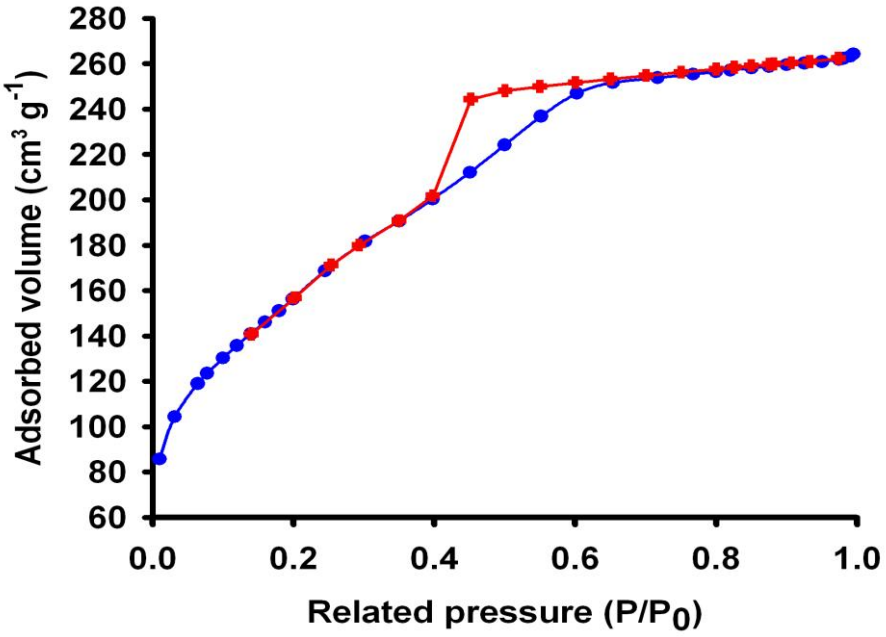

Figure 35. Nitrogen adsorption/desorption isotherms of MOS.

synthesized in CTAB had the largest void fraction in the mesoporous structure, and it had the lowest dielectric constant. Its calculated dielectric constant (1.73) is low enough for the filling of nanotrenches below 20 nm wide. The elastic modulus of MOSs was measured by an atomic force microscopy (AFM) nanoindentation technique. The results were 6.14 respectively, for MOS. The highest value is approximately 1.5 times that of conventional materials such as pure mesoporous silica (ca. 4.0$Nm^{-}2$). A high Young's modulus resulted from crosslinking of TEOS with BTE.[110] The low value for MOS-8 was responsible for the deformation of the mesoporous structure. Nevertheless, it meets the minimum stiffness requirement (<6 N m-2) for nanogap-filling materials.

3.2.2. Fabrication of Mesoporous Organosilica Film with Enhanced Physical Properties Using Sol-gel Process and Vapor Phase Synthesis

We report here the VPS of a low-k, crack-free, mesoporous organosilica (MOS) in a shallow nanotrench with 25 nm width and 400 nm depth (aspect ratio : 16). TEOS and BTE were used as the precursors of the mesoporous silica. BTE created crosslinked molecular structure at synthesized MOS, and reinforeced the physical properties including elastic modulus, dielectric constant. To maximize the concentration of BTE in synthesized MOS, sol-gel precess and VPS method were employed at the same time. Cetyltrimethylammonium bromide (CTAB) was selected for the surfactant. Phosphoric acid was used as the catalyst for the condensation reaction that formed the silica in shallow trenchs.

The overall process of the MOS in shallow trenches of a patterned wafer is represented in Scheme 36. First, the patterned wafer was treated with O2 plasma for 1 min with 20 ccm of gas flow and 100 W power to hydrophilicity on surface. The plasma treated wafer was soaked in precursor solution containing surfactant, BTE and phosphoric acid. After 5 min soaking, shallow trenches were filled with precursor solution because the surface of shallow trenches had hydrophilicity by plasma treatment. The wafer was taken out from

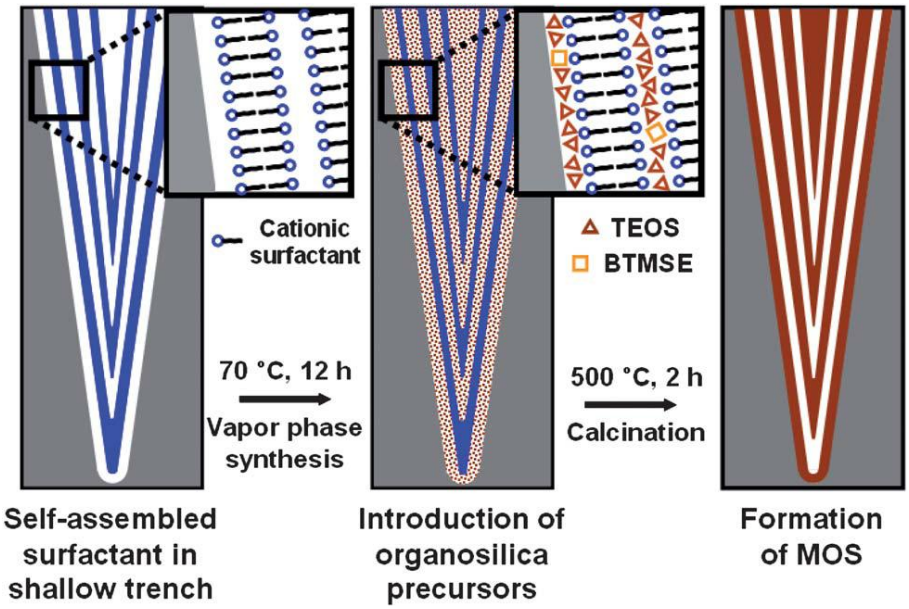

Figure 36. Schematic illustration of the fabrication of mesoporous organosilica using VPS in a shallow trench.

precursor solution and spin coated at 1500 rpm for 15 s to remove excess precursor solution. The wafer was put into the vessel which contained vaporized BTE at 90 ℃ for 1 h. Vaporized BTE was diffused into precursor solution and reacted with dissolved BTE in entire solution by phosphoric acid. The reaction of precursor was condensation reaction. After reaction, the wafer was calcined at 500 ℃ for 2 h to remove excess reagents. The structure of fabricated organosilica was reinforced while calcinations by removal of volatile defects such as hydroxyl and silanol functional groups.

Figure 37 displays field-emission scanning electron microscope (FE-SEM) images of surface of the pristine wafer and the MOS coated wafer. In figure 1a, the wafer has vertically aligned shallow trenches and the width and feature size of them were 25 nm and 25 nm, respectively. There were no significant defects at trenches what were originated from pre-treatment such as cutting, plasma treatment, and washing. This meant that the defects which formed after reaction were certainly occurred by reaction condition. Figure 37b shows surface of the wafer after reaction. The image cleary represent that the trenches of the pristine wafer were covered with synthesized organosilica. MOS had smooth surface and there was no significant defects such as crack and distortion. This meant that the volume reduction of synthesized organosilica did not occurred while condensation reaction. The detailed

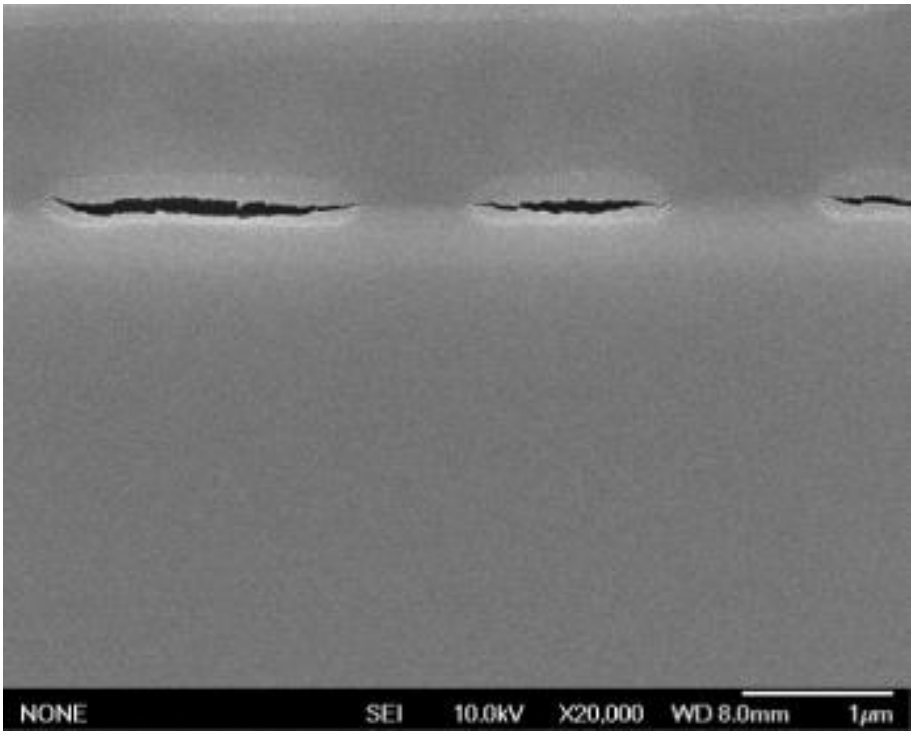

Figure 37. Surfacial FE-SEM images of MOS filled patterned Si wafer.

structure of MOS could not be observed with perpendicular viewpoint.

The cross-sectional FE-SEM images of pristine and MOS-filled wafer (Figure 38) show the MOS which is filling shallow trenches. The pristine wafer had thin walls and reverse-triangle-shaped trenches (Figures 38a) with a width, depth, and feature size of 25 nm, 400 nm, and 25 nm, respectively. Similar with as seen at the perpendicular image, the walls of patterned silicon wafer did not be damaged while reaction. After vapor phase synthesis, shallow trenches of the wafer were filled with synthesized MOS (Figure 38b). The images were investigated using focused ion beam (FIB) and back scattered electrons (BSE) detector. FIB method could etch the wafer vertically by gallium ion and enabled to observe the section of sample. After vertical etching, silicon and silica in the section of sample could not be distinguished because they had same height. However, BSE detector could distinguish silicon and silica by the numbers of components atoms. In BSE detector, heavier atoms appear brighter than lighter atoms. The MOS appears darker than the silicon wafer because it contains atoms that are lighter than silicon, *i.e.*, carbon and oxygen.

Figure 39 represents the TEM images of mesoporous silica which synthesized using vaporized TEOS and BTE as precursors. Compared with mesoporous silica by pure TEOS, significant difference was not observed. The CTAB enabled the formation of well ordered lamellar mesoporous structure for

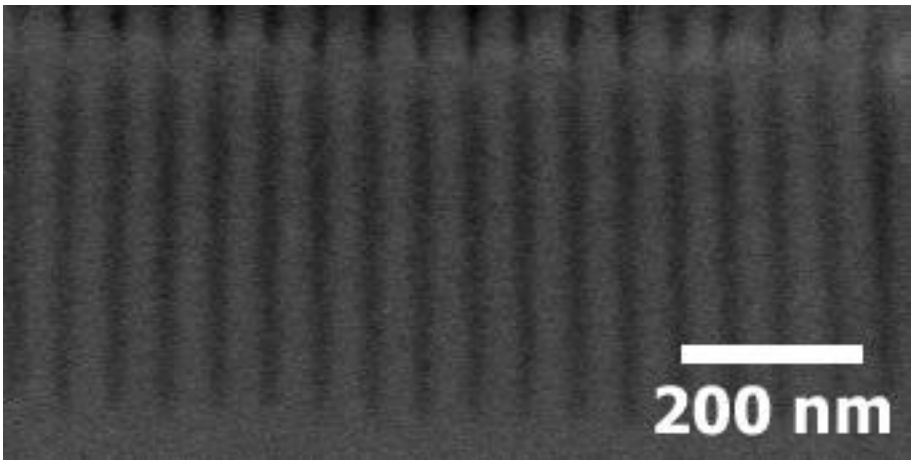

Figure 38. Cross-sectional FE-SEM images of the MOS filled patterned Si wafer.

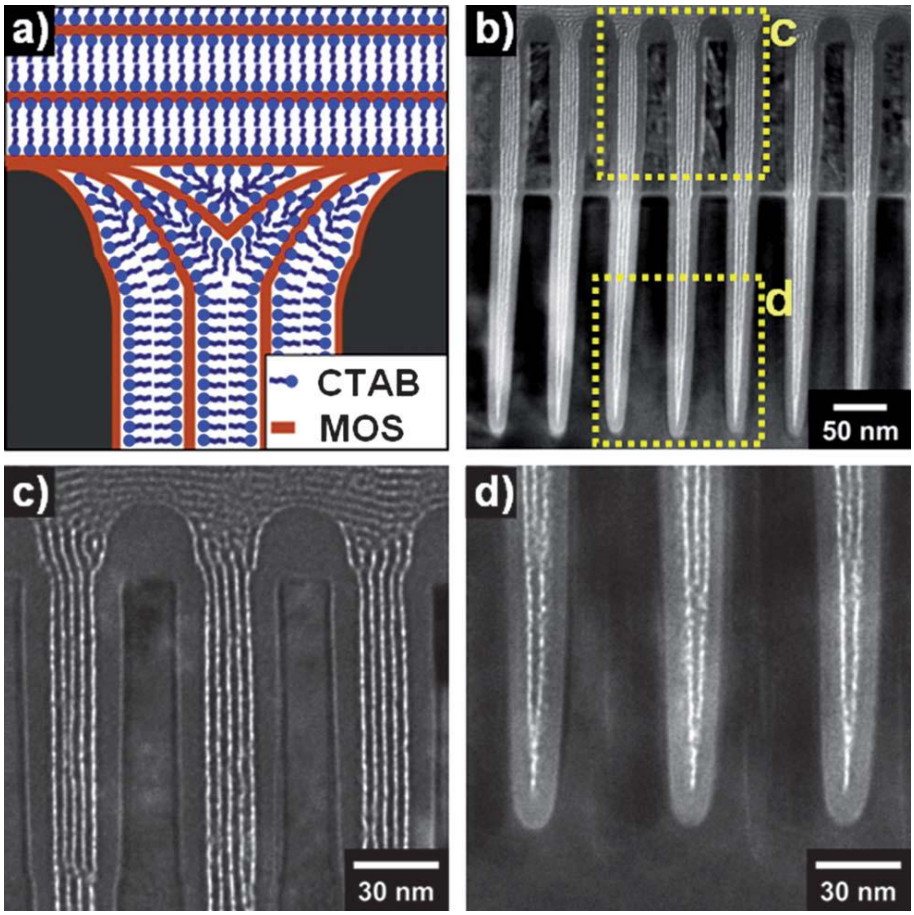

Figure 39. (a) Schematic illustration of the mesostructure of the organosilica layer that was structured by self-assembled CTAB. (b) Overall crosssectional TEM images of patterned Si wafer filled with MOS, (c) and (d) higher magnification of the boxed areas in (b).

MOS. This meant that vaporized TEOS and BTE showed similar behavior in vapor phase and hydrolyzed state. The pore size of the MOS was approximately 3 nm in TEM observation, which agreed well with the pore size data in Table 1 from BET measurement. And this data well matched with the general pore size of mesoporous silica by CTAB as surfactant. Judging from these data, vapor phase synthesis could be applied to fabricated functionalized organosilica with mesoporous structure.

Table 6 shows the chemical composition of MOS compared with silica gel and pristine organosilica. The EDS analyze was employed to measure the weight ratio, and atomic ratio of samples were calculated from the weight ratio and molecular weight. Pure silica gel did not contain carbon elements and atomic ratio of O/Si was 1.95. Also, atomic ratio of O/Si of sol-gel synthesized pristine organosilica and MOS were 1.93 and 1.95, respectively. These atomic value were lower than the theoretical value of silica (O/Si = 2). This may be originated from imperfect molecular structure of samples [19, 20]. The pristine organosilica and MOS contained carbon atoms in those molecular structures. The theoretical atomic ratio of C/Si was 0.61 which was similar with that of pristine organosilica. However, the atomic ratio of C/Si of MOS was 0.55, and it was slightly lower than the theoretical value. This low carbon content of MOS was resulted from different molecular weight of BTE (M.W = 270.43)

and TEOS (M.W = 208.33). BTE is heavier than TEOS, and it make BTE hard to evaporate. Therefore, the supply speed of BTE was slower than TEOS to surface of surfactants solution. It induced lower content of BTE in synthesized MOS than sol-gel synthesized organosilica.

Fig. 41 shows the nitrogen adsorption/desorption isotherms of the synthesized MOSs. For nitrogen adsorption/desorption isotherms measurement, MOS powder samples using CTAB and different BTE ratio were fabricated and collected at the surface of pristine wafers without patterns under the same experimental conditions of the patterned wafer. Approximately 0.1 g of the sample was used for nitrogen adsorption/desorption isotherms measurement. The obtained isotherms had a type IV hysteresis loop according to the Brunauer classification scheme. The inset of Fig. 41 shows the graph of pore-size distribution (PSD) as calculated by the Barrett, Joyner, and Halenda (BJH) method. The Brunauer–Emmett–Teller (BET) surface area of MOS was calculated to be 589.74m2 g 1, and the average pore size value of the MOS was estimated to be 3.04 nm (Table 5). The hysteresis loop and PSD plot indicated that the MOS had open pores.

Table 6. Chemical compositions of synthesized MOSs with various molecular ratio of TEOS and BTE.

	Atomic ratio (%)			C/Si
	C	Si	O	
BTE 100	24.7	25	50.3	1
BTE 90	21.9	28.9	49.2	0.79
BTE 80	19.6	20.4	50	0.67
BTE 70	17.1	32.5	50.4	0.54
BTE 60	14.2	35.2	50.6	0.43
BTE 50	11.5	38.2	50.3	0.33

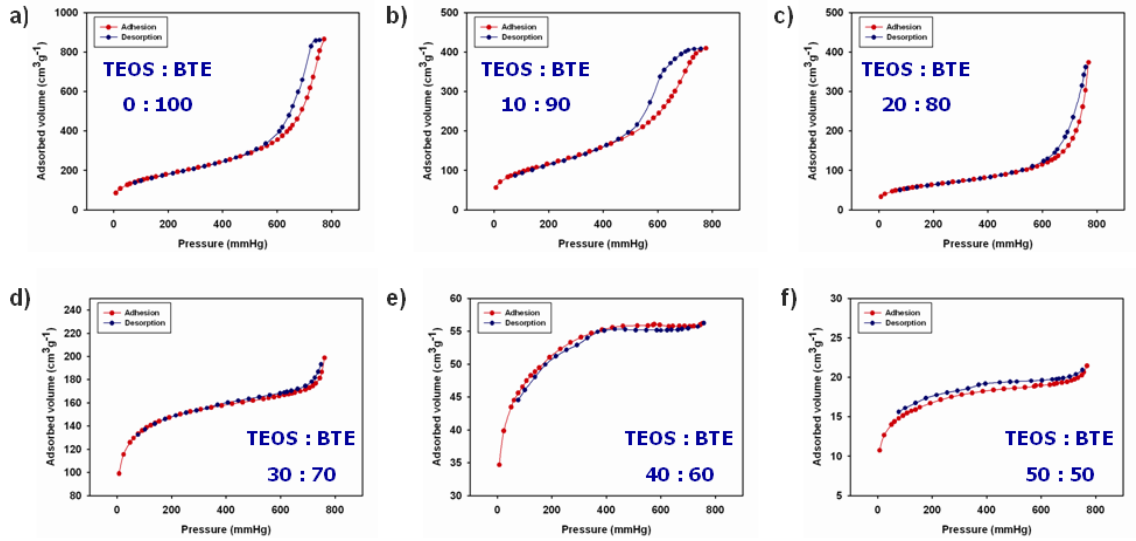

Figure 41. Nitrogen adsorption/desorption isotherms of the POS with a) [TEOS : BTE = 0 : 100], b) [TEOS : BTE = 10 : 90], c) [TEOS : BTE = 20 : 80], d) [TEOS : BTE = 30 : 70], e) [TEOS : BTE = 40 : 60], f) [TEOS : BTE = 50 : 50]

The physical properties of various MOS are summarized in Table 7. Their dielectric constants were also calculated from the dielectric constant of dense silica (ca. 4.0) and the porosity of the MOS as measured by the nitrogen adsorption/desorption isotherm. As shown in Table 1, as the tail spacer length of the surfactant increased from 8 to 16, the calculated dielectric constant decreased from 1.84 to 1.73. According to the d-spacings and the average pore sizes, the wall thicknesses of the MOSs were similar (ca. 1 nm). The MOS synthesized in CTAB had the largest void fraction in the mesoporous structure, and it had the lowest dielectric constant. Its calculated dielectric constant (1.73)

Table 7. Physical properties of MOSs

TEOS (%)	BTE (%)	C contents	Surface area	Porosity	Dielectric constants	Young's modulus
		%	[m3g-1]	[%]	[ε]	[Nm-2]
0	100	15.45	452.09	43.1	2.08	5.24
10	90	12.42	352.63	42.6	2.08	5.11
20	80	9.36	423.90	41.8	2.09	4.99
30	70	6.27	327.43	39.2	2.12	4.83
40	60	3.15	293.89	36.2	2.16	4.42
50	50	1.02	251.29	33.5	2.20	4.11

is low enough for the filling of nanotrenches below 20 nm wide. The elastic modulus of MOSs was measured by an atomic force microscopy (AFM) nanoindentation technique. With high concentration of BTE, the Young's modulus of MOSs increased dramatically. Nevertheless, it meets the minimum stiffness requirement (<6 N m^{-2}) for nanogapfilling materials.

3.2.3. Hygroscopicity Modification of Mesoporous Silica Using Fluorinated Silane Coupling Agent

We report here the VPS of a low-k, crack-free, low hygroscopicity, porous fluroinated organosilica (FOS) in a shallow nanotrench with 25 nm width and 400 nm depth (aspect ratio : 16). TEOS and TEFS were used as the precursors of the mesoporous silica. TEFS played a role of decreaseing hygroscopicity of synthesized organosilica by fluorine atoms [111]. To maximize the concentration of TEFS in synthesized MOS, VPS method was employed. Cetyltrimethylammonium bromide (CTAB) was selected for the surfactant. Phosphoric acid was used as the catalyst for the condensation reaction that formed the silica in shallow trenchs.

The overall synthesis of the FOS is illustrated in Figure 42. First, the silicon wafer was treated with O2 plasma for 1 min with 20 ccm of gas flow and 100 W power to hydrophilicity on surface. The plasma treated wafer was soaked in catalyst solution containing sodium hydroxide. In this step, water was excluded from reagents because of its strong reactivity with TEFS. After 5 min soaking, the wafer was taken out from catalyst solution, and was spin coated at 3000 rpm for 30 s to remove excess catalyst solution. Before reaction, precursors were vaporized in a vessel at 70 ℃ for 1 h. Induced from boiling

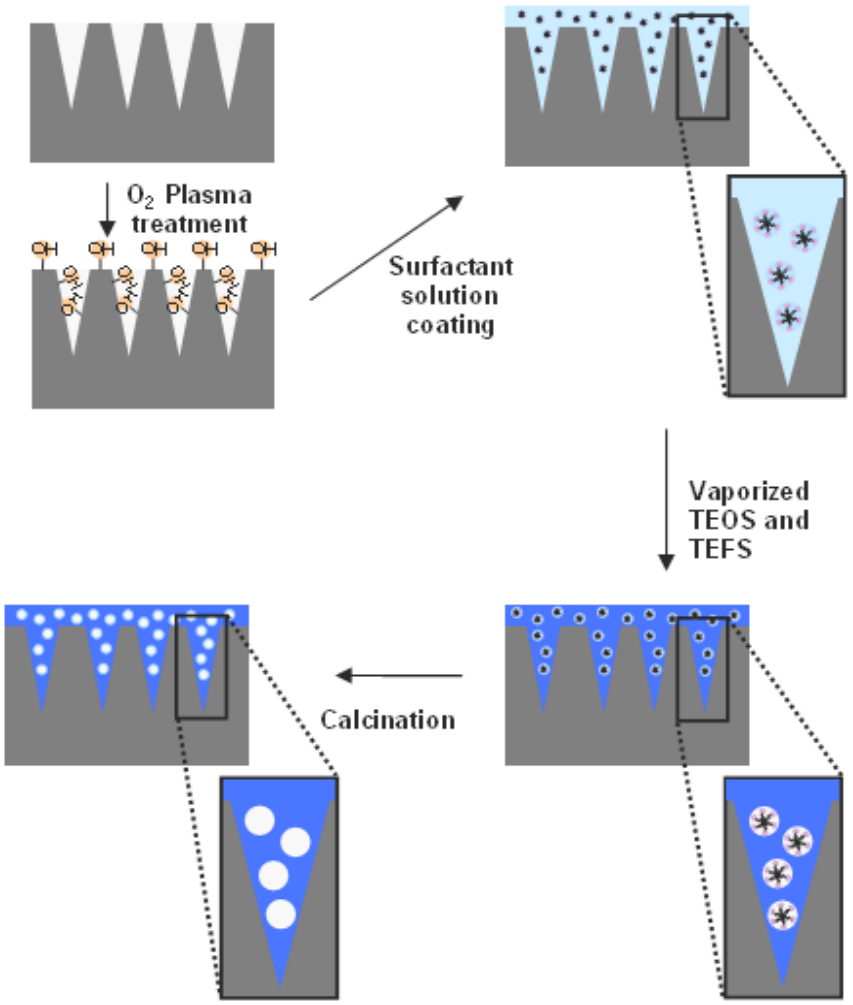

Figure 42. Schematic illustration of the synthesis of porous fluorinated organosilica using VPS in a shallow trench.

points the vapor pressure of TEFS is higher than that of TEOS. Therefore, enough precursors were vaporized in a vessel. The wafer was taken in the vessel that saturated with vaporized precursor. Vaporized precursor was hydrolyzed to silanol from surface of spin coated catalyst solution at 70 ℃ for 12 h. Hydrolyzed precursor diffused to entire solution, and reacted with catalyst. The reaction of precursor was condensation reaction. After reaction, the wafer was calcined at 500 ℃ for 2 h to remove excess reagents.

Figure 43 displays field-emission scanning electron microscope (FE-SEM) images of surface and a section of the pristine wafer and the FOS coated wafer. The FE-SEM images clearly show that the trenches of the pristine wafer were covered with synthesized silica. In figure 43a, the wafer has vertically aligned shallow trenches and the width and feature size of them were 25 nm and 25 nm, respectively. There were no significant defects at trenches what were originated from pre-treatment such as cutting, plasma treatment, and washing. Figure 43b shows surface of the wafer after reaction. The nanopattern was fully covered with FOS and trenches were could not be observed with perpendicular viewpoint. FOS had smooth surface and there was no significant defects such as crack and distortion.

Figure 44 displays cross-sectional field-emission scanning electron microscope (FE-SEM) images of the FOS-filled wafer. The FE-SEM images

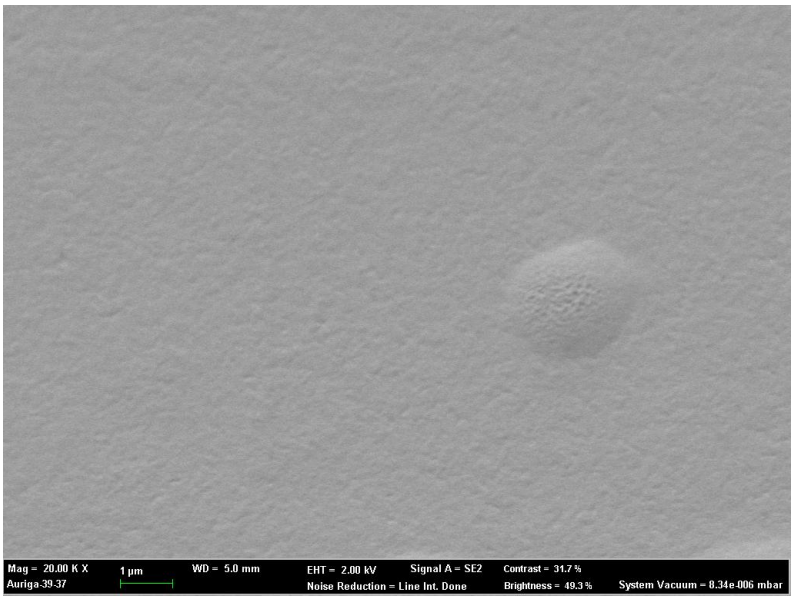

Figure 43. Surfacial SEM image of FOS.

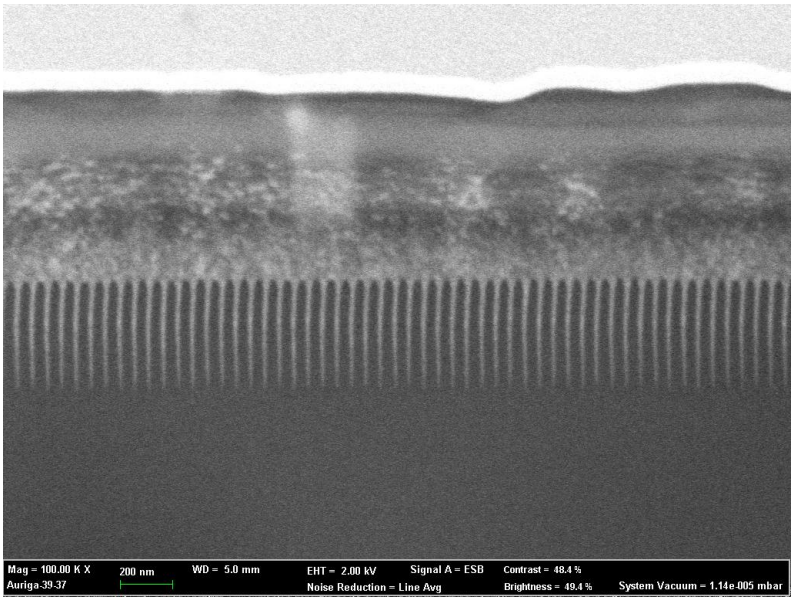

Figure 44. Cross-sectional SEM image of FOS by FIB and BSE detector.

clearly show the vertical reverse- triangular-shaped trenches, which had 25 nm width and 400 nm depth with a feature size of 25 nm. For Figure 44b, a focused ion beam (FIB) was used to image the cross-section of the FOS-filled wafer; a back-scattered electron (BSE) detector was used to distinguish silicon from the FOS. The synthesized FOS indicates darker than the crystalline silicon of the wafer in the BSE detector because silicon is heavier than the carbon and oxygen atoms in the FOS. Dark regions in middle of Si wafer represented silica layer that originated from 2-step dry etch in the wafer preparation. To the best of our knowledge, there are no reports that representing the fabrication of mesoporous silica in shallow trench with dimensions less than 50 nm. Under our experimental condition, the trenches and walls with 25 nm width did not collapse without significant shrinkage during condensation reaction.

Figure 45 represents the TEM images of mesoporous silica which synthesized using vaporized TEOS and TEFS as precursors. Compared with MOS from pure TEOS, significant difference was not observed. The CTAB enabled the formation of well ordered hexagonal mesoporous structure for FOS. This meant that vaporized TEOS and TEFS showed similar behavior in vapor phase and hydrolyzed state. The pore size of the FOS was approximately 3 nm in TEM observation, which agreed well with the pore size data in Table 7 from

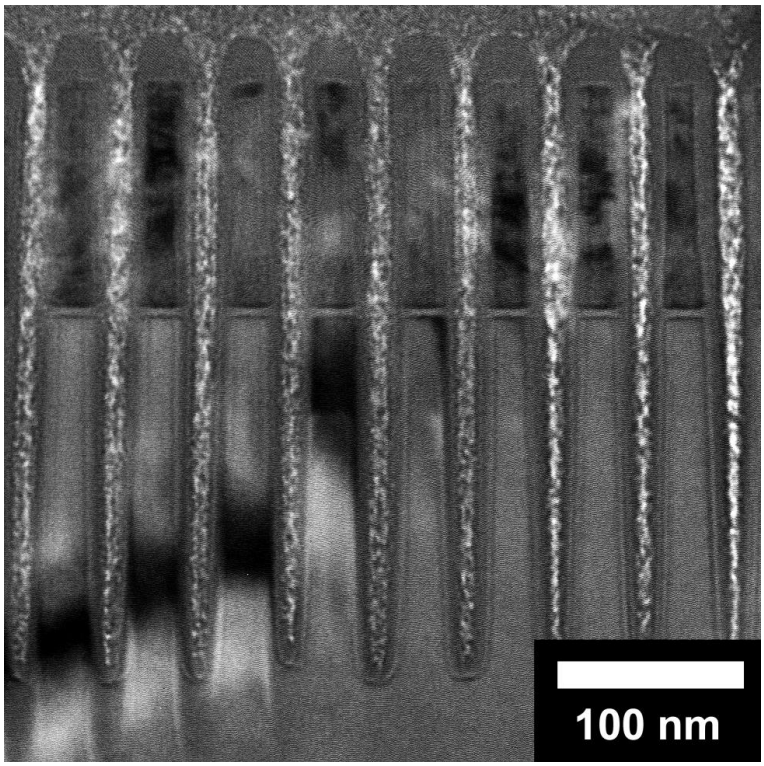

Figure 45. Cross-sectional TEM image of FOS

BET measurement. And this data well matched with the general pore size of mesoporous silica by CTAB as surfactant. Judging from these data, vapor phase synthesis could be applied to fabricated functionalized organosilica with mesoporous structure.

Table 8 shows the chemical composition of MOS compared with silica gel and pristine organosilica. The EDS analyze was employed to measure the weight ratio, and atomic ratio of samples were calculated from the weight ratio and molecular weight. Pure silica gel did not contain carbon elements and atomic ratio of O/Si was 1.95. Also, atomic ratio of O/Si of sol-gel synthesized pristine organosilica and MOS were 1.93 and 1.95, respectively. These atomic value were lower than the theoretical value of silica (O/Si = 2). This may be originated from imperfect molecular structure of samples [19, 20]. The pristine organosilica and MOS contained carbon atoms in those molecular structures. The theoretical atomic ratio of C/Si was 0.61 which was similar with that of pristine organosilica. However, the atomic ratio of C/Si of MOS was 0.55, and it was slightly lower than the theoretical value. This low carbon content of MOS was resulted from different molecular weight of TEFS (M.W = 270.43) and TEOS (M.W = 208.33). TEFS is heavier than TEOS, and it make TEFS hard to evaporate. Therefore, the supply speed of TEFS was slower than TEOS to surface of surfactants solution. It induced lower content of TEFS in

Table 8. Chemical compositions of silica gel, pristine organosilica (50 wt% BTSE) and POS.[a]

	Atomic ratio (%)			F/Si	F/Si
	F	Si	O		
Silica gel	-	33.9	66.1	1.95	-
FOS	15.5	28.6	55.9	1.95	0.54

synthesized MOS than sol-gel synthesized organosilica.

Fig. 47 shows the nitrogen adsorption/desorption isotherms of the synthesized FOS. For nitrogen adsorption/desorption isotherms measurement, FOS powder samples using CTAB, were fabricated and collected at the surface of pristine wafers without patterns under the same experimental conditions of the patterned wafer. Approximately 0.1 g of the sample was used for nitrogen adsorption/desorption isotherms measurement. The obtained isotherms had a type IV hysteresis loop according to the Brunauer classification scheme.10The inset of Fig. 47 shows the graph of pore-size distribution (PSD) as calculated by the Barrett, Joyner, and Halenda (BJH) method. The Brunauer–Emmett–Teller (BET) surface area of FOS was calculated to be 589.74m2 g 1, and the average pore size value of the FOS was estimated to be 3.04 nm (Table 9). The hysteresis loop and PSD plot indicated that the FOS had open pores.

TGA measurement was used to mesure the hydroscopicity of FOS. As could be seen at Figure 48, the weight of FOSs decreased while heating. These decreases were originated from adsorbed water molecules in hydroscopic functional groups such as hydroxyl group in FOSs. When the FOSs were heated, at apploxymately 50 °C, the water molecules started to evaporate and it continued to about 100 °C. The weight losses were decreased with the increase of molecular ratio of TEFS in FOS. This meant that fluorine atoms in

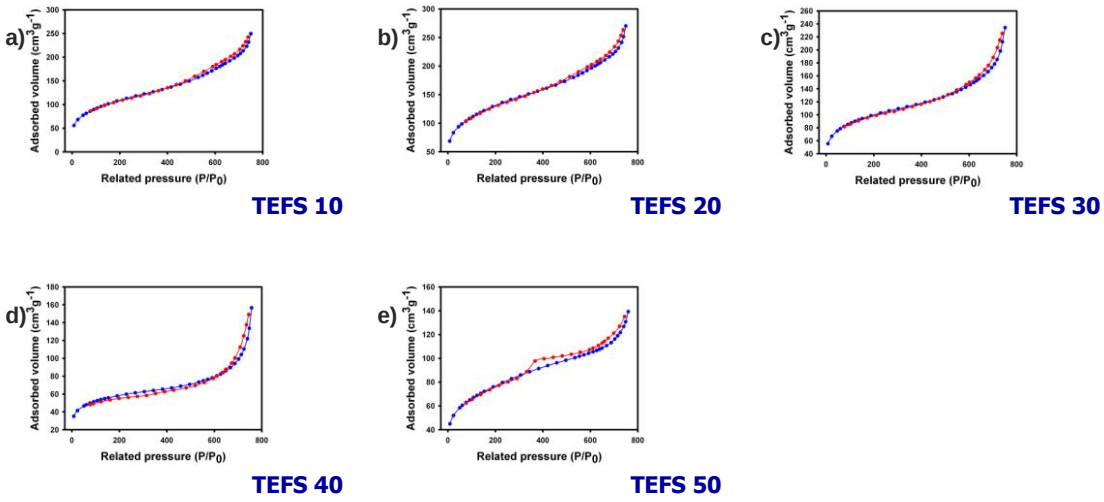

Figure 47. Nitrogen adsorption/desorption isotherms of FOSs.

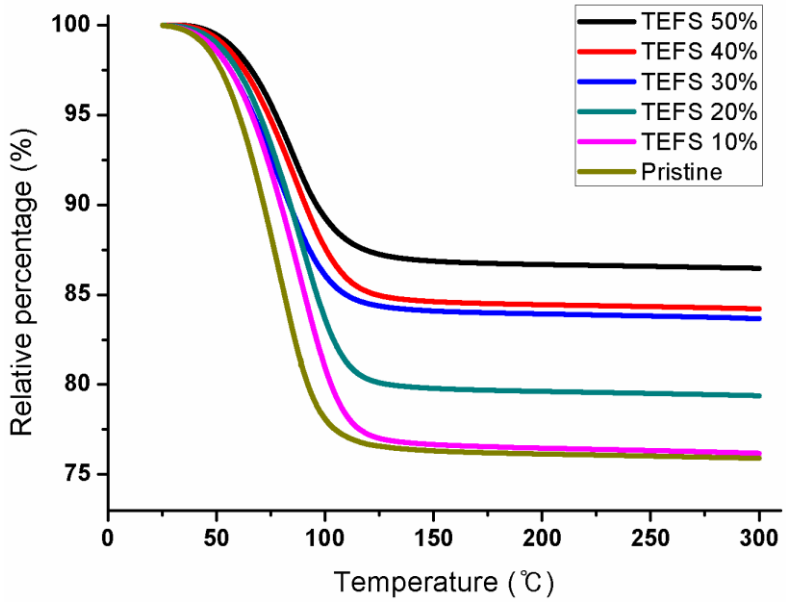

Figure 48. TGA data of FOSs synthesized by various molecular ratio between TEOS and TEFS.

TEFS did not adsorbed water molecules and they block the absorbtion of water molecules by hydroxyl groups. Therefore, the introduction of TEFS in organosilica was effective to reduce the hydroscopicity of organosilica dielectric materials.

The physical properties of various FOS are summarized in Table 9. Their dielectric constants were also calculated from the dielectric constant of dense silica (ca. 4.0) and the porosity of the FOS as measured by the nitrogen adsorption/desorption isotherm. Its calculated dielectric constant (1.73) is low enough for the filling of nanotrenches below 20 nm wide. The elastic modulus of FOSs was measured by an atomic force microscopy (AFM) nanoindentation technique. The results were 6.14, 6.61, and 6.84 N $m^{-}2$, respectively, for FOS-8, FOS-12, and FOS-16. The highest value is approximately 1.5 times that of conventional materials such as pure mesoporous silica (ca. 4.0$Nm^{-}2$). A high Young's modulus resulted from crosslinking of TEOS with TEFS.[5] The low value for FOS-8 was responsible for the deformation of the mesoporous structure. Nevertheless, it meets the minimum stiffness requirement (<6 N $m^{-}2$) for nanogapfilling materials.

Table 9. Physical properties of FOS with various molecular ratio between TEOS and TEFS.

TEOS (%)	TEFS (%)	F contents	Surface area	Porosity	Dielectric constants	Young's modulus
		%	[m3g-1]	[%]	[ε]	[Nm-2]
100	0	-	589.74	55.9	2.21	3.42
90	10	3.15	521.90	48.6	2.29	3.04
80	20	6.27	430.63	47.8	2.28	2.90
70	30	9.36	313.11	45.2	2.30	2.71
60	40	12.42	279.91	44.2	2.29	2.55
50	50	15.45	230.84	43.5	2.28	2.43

4. CONCLUSIONS

1. Silica thin film was successfully synthesized from spin coated phosphoric acid solution and vaporized precursor. The synthesis was occurred in nanoscale trenches and there were no significant defects such as crack. This was because of perfectly filled trenches by catalyst solution and continuous supply of hydrolyzed precursor from vaporized precursors. In case of sol-gel solution, when reaction occurred, condensation reaction accompanied volume reduction. Many defects were formed by volume reduction. Moreover, synthesized STF showed smooth surface which good to apply on CMP process.
2. Mesoporous silica films were fabricated in shallow trenches by surfactant solution and vaporized precursors. Moreover, synthesized MOSs had well ordered mesostructures and could fill extremely narrow gaps, without defects such as cracks and trench gradients. The synthesized MOSs had ultra-low dielectric constants because of their high porosities. The mesoporous structures were influenced by species of surfactants. On this basis, it is anticipated that MOSs have sufficient dielectric characteristics for use in IC chips.
3. Highly porous silica was synthesized in the trenches of patterned silicon wafers using VPS. The synthesized POS had a highly porous structure and

filled narrow trenches without defects. The POS had a low dielectric constant because of its high porosity.. The physical properties of the POS film are sufficient for use in IC chips. In addition, POS can be used as supports for the catalysts, filter of high-pressure liquid chromatography, and filler of polymer composites because of its high porosity and stability

4. Mesoporous organosilica was successfully filled the nanoscale patterns of silicon wafer using dual precursor. The synthesized MOS showed enhanced physical properties compared with the mesoporous silica consisted by pure TEOS. This enhancement was originated from the crosslinking reaction by BTE. In addition, higher molecular ratio of BTE could be accomplished by using sol-gel process and VPS at the same time. BTE in sol-gel solution could easily form organosilica in shallow trenches. The MOS had a low dielectric constant because of its high porosity; crosslinking provided a relatively high Young's modulus. The physical properties of the POS film are sufficient for use in IC chips.
5. Fluorinated organosilica was synthesized in nanoscale trenches using vaporized fluorinated silane coupling agent and VPS. The fabricated FOS showed low hygroscopicity because of substitution between hydroxyl group and fluorinated group. The FOS had a low dielectric constant because of its high porosity; and TEFS as precursor. The additional

mechanical properties should be improved by introducing of crosslinking agents such as BTE.

In summary, various porous organosilica films in shallow trenches were successfully fabricated using vapor phase synthesis. The formation of dense silica by VPS proofed the new method which can replace the CVD and sol-gel method. The usage of cationic and nonionic surfactants made the mesopores in structure of silica, and this made the enhanced physical properties originated from air void. In the view of controlling precursors, crosslinking agent and fluorinated silane were used to make the physical properties distinguished. Therefore, synthesized porous organosilica films can be applied to manufacturing process of IC chips as low-k materials. Also, because of large surface area and fine mechanical properties, porous organosilica film having an ordered mesoporous structure and it can provide a novel platform for applications such as high-performance separation filters, supports for catalysts, and high-sensitivity biosensors.

REFERENCES

[1] K. Landskron, B. D. Hatton, G. A. Ozin, *Science* **2003**, *302*, 266.

[2] R. A. Pai, R. Humayun, M. T. Schulberg, A. Sengupta, J.-N. Sun,J. J. Watkins, *Science* **2004**, *303*, 507.

[3] K. S. Novoselov, A. K. Geim, S. V. Morozov, D. Jiang, Y. Zhang, S. V. Dubonos, I. V. Grigorieva, A. A. Firsov, *Science*, **2004**, *306*, 666.

[4] S. Yang, P. Mirau, C. S. Pai, O. Nalamasu, E. Reichmanis, J. C. Pai, S. Y. Obeng, J. Seputro, E. K. Lin, H.-J. Lee, J. Sun, D. W. Gidley, *Chem. Mater.* **2002**, *14*, 369.

[5] M. I. Katsnelson, *Materials Today*, **2007**, *10*, 20.

[6] A. K. Geim, K. S. Novoselov, *Nature Mater.*, **2007**, *6*, 183.

[7] D. R. Dreyer, R. S. Ruoff, C. W. Bielawski, *Angew. Chem. Int. Ed.*, **2010**, *49*, 9336.

[8] H. Dong, M. A. Brook, J. D. Brennan, *Chem. Mater.* **2005**, *17*, 2807.

[9] M. S. Dresselhaus, G. Dresselhaus, *Adv. Phys.*, **1981**, *30*, 139.

[10] P. Yang, G. Wirnsberger, H. C. Huang, S. R. Cordero, M. D. McGehee, B. Scott, T. Deng, G. M. Whitesides, B. F. Chmelka, S. K. Buratto, G. D. Stucky, *Science* **2000**, *287*, 465.

[11] H. P. Boehm, R. Setton, E. Stumpp, *Carbon*, **1986**, *24*, 241.

[12] W.-C. Chen, L.-H. Lee, B.-F. Chen, C.-T. Yen, *J. Mater. Chem.* **2002**,

12, 3644.

[13] P. M. Stefan, M. L. Shek, I. Lindau, W. E. Spicer, L. I. Johansson, F. Herman, R. V. Kasowski, G. Brogen, *Phys. Rev. B*, **1984**, *29*, 5423.

[14] H.-C. Kim, G.Wallraff, C. R. Kreller, S. Angelos, V. Y. Lee,W. Volksen, R. D. Miller, *Nano Lett.* **2004**, *4*, 1169.

[15] A. Nagashima, K. Nuka, H. Itoh, T. Ichinokawa, C. Oshima, S. Otani, *Surf. Sci.*, **1993**, *291*, 93.

[16] H.-C. Kim, C. R. Kreller, K. A. Tran, V. Sisodiya, S. Angelos, G. Wallraff, S. Swanson, R. D. Miller, *Chem. Mater.* **2004**, *16*, 4267.

[17] R. F. Cook, E. G. Liniger, *J. Electrochem. Soc.* **1999**, *146*, 4439.

[18] N. A. Kholin, E. V. Rut'kov, A. Y. Tontegode, *Surf. Sci.*, **1984**, *139*, 155.

[19] E. P. Guyer, R. H. Dauskardt, *Nat. Mater.* **2004**, *3*, 53.

[20] H. Zi–Pu, D. F. Ogletree, M. A. Van Hove, G. A. Somorjai, *Surf. Sci.*, **1987**, *180*, 433.

[21] C. E. Bouldin, W. E. Wallace, G. W. Lynn, S. C. Roth, W. L. Wu, *J. Appl. Phys.* **2000**, *88*, 691

[22] C. Berger, Z. M. Song, T. B. Li, X. Li, A. Y. Ogbazghi, R. Feng, Z. T. Dai, A. N. Marchenkov, E. H. Conrad, P. N. First, W. A. de Heer, *J. Phys. Chem. B*, **2004**, *108*, 19912.

[23] W.-L. Wu, H.-C. Liou, *Thin Solid Films* **1998**, *312*, 73.

[24] D. D. L. Chung, *J. Mater. Sci.*, **1987**, *22*, 4190.

[25] W.-L. Wu, W. E. Wallace, E. K. Lin, G. W. Lynn, C. J. Glinka, E. T. Ryan, H.-M. Ho, *J. Appl. Phys.* **2000**, *87*, 1193

[26] H. J. Lee, C. L. Soles, D. W. Liu, B. J. Bauer, W. L. Wu, *J. Polym. Sci. Part B* **2002**, *40*, 2170.

[27] C. Soldano, A. Mahmood, E. Dujardin, *Carbon*, **2010**, *48*, 2127.

[28] H. J. Lee, C. L. Soles, D. W. Liu, B. J. Bauer, E. K. Lin, W. L. Wu, A. Grill, *J. Appl. Phys.* **2004**, *95*, 2355.

[29] Y. Hernandez, V. Nicolosi, M. Lotya, F. M. Blighe, Z. Sun, S. De, I. T. McGovern, B. Holland, M. Byrne, Y. K. Gun'ko, J. J. Boland, P. Niraj, G. Duesberg, S. Krishnamurthy, R. Goodhue, J. Hutchison, V. Scardaci, A. C. Ferrari, J. N. Coleman, *Nat. Nanotechnol.*, **2008**, 3, 563.

[30] H.-J. Kim, J.-K. Lee, J. B. Kim, E. S. Park, S. J. Park, D. Y. Yoo, D. Y. Yoon, *J. Am. Chem. Soc.* **2001**, *123*, 12 121.

[31] O. C. Compton, S. T. Nguyen, *Small*, **2010**, *6*, 711.

[32] S. Park, J. An, I. Jung, R. D. Piner, S. J. An, X. Li, A. Velamakanni, R. S. Ruoff, *Nano Lett.*, **2009**, *9*, 1593.

[33] L.-H. Lee, W.-C. Chen, W.-C. Liu, *J. Polym. Sci. Part A* **2002**, *40*, 1560.

[34] Y. Shao, J. Wang, M. Engelhard, C. Wang, Y. Lin, *J. Mater. Chem.*, **2010**, *20*, 743.

[35] L. Zheng, A. J. Waddon, R. J. Farris, E. B. Coughlin, *Macromolecules* **2002**, *35*, 2375.

[36] V. Strong, S. Dubin, M. F. El-Kady, A. Lech, Y. Wang, B. H. Weiller, R. B. Kaner, *ACS Nano*, **2012**, *6*, 1395.

[37] G.-M. Kim, H. Qin, X. Fang, F. C. Sun, P. T. Mather, *J. Polym. Sci. Part B* **2003**, *41*, 3299.

[38] W. A. de Heer, C. Berger, X. Wu, M. Sprinkle, Y. Hu, M. Ruan, J. A. Stroscio, P. N. First, R. Haddon, B. Piot, C. Faugeras, M. Potemski, J.-S. Moon, *J. Phys. D: Appl. Phys.*, **2010**, *43*, 374007.

[39] A. Strachota, I. Kroutilova, J. Kovarova, L. Matejka, *Macromolecules* **2004**, *37*, 9457.

[40] V. Y. Aristov, G. Urbanik, K. Kummer, D. V. Vyalikh, O. V. Molodtsova, A. B. Preobrajenski, A. A. Zakharov, C. Hess, T. Haenke, B. Buechner, I. Vobornik, J. Fujii, G. Panaccione, Y. A. Ossipyan, M. Knupfer, *Nano Lett.*, **2010**, *10*, 992.

[41] D. A. Loy, J. P. Carpenter, T. M. Alam, R. Shaltout, P. T. Dorhout, J. Greaves, J. H. Small, K. J. Shea, *J. Am. Chem. Soc.* **1999**, *121*, 5413.

[42] Y. Dedkov, A. Shikin, V. Adamchuk, S. Molodtsov, C. Laubschat, A.

Bauer, G. Kaindl, *Phys. Rev. B*, **2001**, *64*, 035405.

[43] W. Norman, J. H. Melvin, *J. Am. Chem. Soc.* **1947**, *69*, 803.

[44] Y. S. Dedkov, M. Fonin, C. Laubschat, *Appl. Phys. Lett.*, **2008**, *92*, 052506.

[45] S. Bae, H. Kim, Y. Lee, X. Xu, J.-S. Park, Y. Zheng , J. Balakrishnan, T. Lei, H. Ri Kim, Y. I. Song, Y.-J. Kim, K. S. Kim, B. Ozyilmaz, J.-H. Ahn, B. H. Hong, S. Iijima, *Nat. Nanotechnol.*, **2010**, *5*, 574.

[46] J. Liu, J. R. Bontha, A. Y. Kim, S. Baskaran, *MRS Bull*. **1996**, *431*, 245.

[47] A. Reina, X. Jia, J. Ho, D. Nezich, H. Son, V. Bulovic, M. S. Dresselhaus, J. Kong, *Nano Lett.*, **2009**, *9*, 30.

[48] G. Lopez, E. Mittemeijer, *Scr. Mater*., **2004**, *51*, 1.

[49] P. J. Bruinsma, J. R. Bontha, J. Liu, S. Baskaran, US Patent 5 922 299, 1999

[50] K. Yan, H. Peng, Y. Zhou, H. Li, Z. Liu, *Nano Lett.*, **2011**, *11*, 1106.

[51] Y. Lu, R. Ganguli, C. A. Drewien, M. T. Anderson, C. J. Brinker, W. Gong, Y. Guo, H. Soyez, B. Dunn, M. H. Huang, J. I. Zink, *Nature* **1997**, *389*, 364.

[52] J. Wu, W. Pisula, K. Muellen, *Chem. Rev.*, **2007**, *107*, 718.

[53] X. Yang, X. Dou, A. Rouhanipour, L. Zhi, H. J. Rader, K. Müllen, *J. Am. Chem. Soc.*, **2008**, *130*, 4216.

[54] D. Zhao, P. Yang, N. Melosh, J. Feng, B. F. Chmelka, G. D. Stucky, *Adv. Mater*. **1998**, *10*, 1380.

[55] X. Yan, X. Cui, L.-s. Li, *J. Am. Chem. Soc.*, **2010**, *132*, 5944.

[56] D. M. Smith, J. Anderson, C. C. Cho, B. E. Gnade, *Mater. Res. Soc. Symp. Proc.* **1995**, *371*, 261..

[57] W. H. Lee, J. Park, S. H. Sim, S. B. Jo, K. S. Kim, B. H. Hong, K. Cho, *Adv. Mater.*, **2011**, *23*, 1752.

[58] D. M. Smith, J. Anderson, C. C. Cho, G. P. Johnston, S. P. Jeng, *Mater. Res. Soc. Symp. Proc*. **1995**, *381*, 261.

[59] H. Ni, X. Li, *Nanotechnology*, **2006**, *17*, 3591.

[60] S. Hengsberger, A. Kulik, P.h. Zysset, *Bone*, 2002, *30*, 178.

[61] C. Jin, J. D. Luttmer, D. M. Smith, T. A. Ramos, *Mater. Res. Bull*. **1997**, *10*, 39.

[62] H. Yang, A. Kuperman, N. Coombs, S. Mamiche-Afara, G. A. Ozin, *Nature* **1996**, *379*, 703.

[63] M.-H. Jo, H.-H. Park, D.-J. Kim, S.-H. Hyun, S.-Y Choi, J.-T. Paik, *J. Appl. Phys*. **1997**, *82*, 1299..

[64] K. Domansky , J. Liu, L. Q. Wang , M.H. Engelhard, S. Baskaran, *J. Mater.* **2001**, *16*, 2810.

[65] X. Li, X. Wang, L. Zhang, S. Lee, H. Dai, *Science*, **2008**, *319*, 1229.

[66] S. J. Kang, B. Kim, K. S. Kim, Y. Zhao, Z. Chen, G. H. Lee, J. Hone, P. Kim, C. Nuckolls, *Adv. Mater.*, **2011**, *23*, 3531.

[67] S. Lee, B. J. Kim, H. Jang, S. C. Yoon, C. Lee, B. H. Hong, J. A. Rogers, J. H. Cho, J. Ahn, *Nano Lett.*, **2011**, *11*, 4642.

[68] J. Lin, X. Wang, *Polymer*, **2007**, *48*, 318.

[69] C. Huang, S. Wu, C. Tsai, W. Liu, *Thin Solid Films*, **2013** *529*, 292.

[70] Y. Ohno, K. Maehashi, Y. Yamashiro, K. Matsumoto, *Nano Lett.*, **2009**, *9*, 3318.

[71] S. Yang, P. Mirau, C. S. Pai, O. Nalamasu, E. Reichmanis, J. C. Pai, S. Y. Obeng, J. Seputro, E. K. Lin, H.-J. Lee, J. Sun, D. W. Gidley, *Chem. Mater*. **2002**, *14*, 369

[72] M. R. Vengatesan, S. Devaraju, K. Dinakaranb. M. Alagar, *J. Mater. Chem*.**2012**, *22*, 7559

[73] E. P. Guyer. R. H. Dauskardt, *Nature materials* **2004**, *4*, 53;

[74] W. Volksen, R. D. Miller, G. Dubois, *Chem. Rev*. **2010**, *110*, 56.

[75] N. Ahner, S.E. Schulz, F. Blaschta, M. Rennau, *Microelectronic Engineering* **2007**, *84*, 2606

[76] M. D. Stoller, S. Park, Y. Zhu, J. An, R. S. Ruoff, *Nano Lett.*, **2008**, *8*, 3498.

[77] H. T. Kim, B. S. Kwon, S. I. Kim, N.-E. Lee, J. H. You, J. H. Han, J. W.

Shon, *J. Korean Phys. Soc*. **2008**, *53*, 1479

[78] J. Yan, T. Wei, B. Shao, Z. Fan, W. Qian, M. Zhang, F. Wei, *Carbon*, **2010**, *48*, 487.

[79] K. Trivedi, C. Floresca, S. Kim, H. Kim, D. Kim, J. Kim, M. J. Kim, W. Hu, *J. Vac. Sci. Technol. B* **2009**, *27*, 3145

[80] C. Yang, A. Cho, F. Pan, T. Tsai, K. Chao, *Adv. Mater.* **2001**, *13*, 1099; L. Nicole, C. Boissie`re, D. Grosso, A. Quach C.Sanchez, *J. Mater. Chem.* **2005**, *15*, 3598.

[81] N. Nishiyama, S. Tanaka, Y. Egashira, Y. Oku, K. Ueyama, *Chem. Mater*. **2003**, *15*, 1006

[82] S. Tanaka, M. P. Tate, N. Nishiyama, K. Ueyama, H. W. Hillhouse, *Chem. Mater*. **2006**, *18*, 5461

[83] T. Maruo, K. Nagata, N. Nishyama, Y. Egashira, K. Ueyama, *J.Colloid Iinterface Sci* **2008**, *328*, 120.

[84] H. W. Ro, K. Char, E. Jeon, H. J. Kim, D. Kwon, H. J. Lee, J. K. Lee, H. W. Rhee, C. L. Soles, D. Y. Yoon, *Adv. Mater*. **2007**, *19*, 705

[85] M. S. Oliver, G. Dubois, M. Sherwood, D. M. Gage, R. H. Dauskardt, *Adv. Funct. Mater*. **2010**, *20*, 2884

[86] K-S. Chang, T. Yoshioka, M. Kanezashi, T. Tsurua. K-L. Tung, *Chem. Commun*. **2010**, *46*, 9140

[87] C. Urata, H. Yamada, R. Wakabayashi, Y. Aoyama, S. Hirosawa, S. Arai, S. Takeoka, Y. Yamauchi, K. Kuroda, *J. Am. Chem. Soc*. **2011**, *133*, 8102.

[88] K. J. Lee, J. H. Oh, Y. Kim, J. Jang, *Adv.Mater*. **2006**, *18*, 2216.

[89] K. J. Lee, S. H. Min, J. Jang, *Chemistry - A European Journal*. **2009**, *15*, 2491.

[90] K. J. Lee , S. H. Min , J. Jang. *Small* **2010**, *21*, 2378.

[91] K. J. Lee, S. H. Min, H. Oh, J. Jang, *Chem. Commun*. **2011**, *47*, 9447.

[92] D. F. Rohlfing, A. Kuhn, *Carbon*, **2006**, *44*, 1942.

[93] Y. Yang, J. H. Lee, T. H. Kim, S. J. Choi, S. J. Choi, T. Chang, S. Kim, D. Kim, H. Kim, Y. Kim, S.-K. Chae, J. H. Kim, *J. Photopolym. Sci. Technol*. **2010**, *2*, 259.

[94] J. H. Kim, *J. Photopolym. Sci. Technol*. **2009**, *5*, 615.

[95] G. I. Goldstein, D. E. Newbury, P. Echlin, D. C. Joy, C. Fiori, E. Lifshin, Scanning electron microscopy and x-ray microanalysis, Plenum Press, New York, USA 1981.

[96] K. Mosig, *Microelectron. Eng*., **2002**, *64*, 11

[97] M. Rasco, *IEEE Intl. Interconnect Tech. Conf. Proc*., **2002**, 113.

[98] S. J. Gregg, K. S. W. Sing, in Adsorption, Surface Area and Porosity, 2nd Edn., Academic Press, London, UK 1982, Ch. 1.

[99] F. Goethals, I. Ciofi, O. Madia, K. Vanstreels, M.R. Baklanov, C. Detavernier, P.V.D. Voort, I. V. Driessche, *J. Mater. Chem*. **2012**, *22*, 8281.

[100] D.C. Arnold, A. Blake, A. Quinn, D. Lacopino, J.M. Tobin, C. Omahony, J.D. Holmes, M.A. Morris, *IEEE Transactions on Nanotechnology*, **2011**, *11*, 451.

[101] Y. Chang, W. Chang, J. Huang, J. Leu, Y. Cheng, *Thin Solid Films* **2013**, *528*, 67.

[102] J. Lee, D.K. Kim, G.J. Min, I. Chung, *Thin Solid Films*, **2012**, *520*, 5007.

[103] H. Zou, S. Wu, J. Shen, *Chemical Reviews*, **2008**, *108*, 3893.

[104] W. Wang, D. Grozea, A. Kim, D.D. Perovic, G.A. Ozin, *Adv. Mater*. **2010**, *22*, 99.

[105] H. Oh, J.H. Kim, J. Jang, *J. Mater. Chem*. **2012**, *22*, 21828.

[106] Y. Huang, S. Wu, H. Lin, C. Kuo, S. Chang, D. Hong, C. Wu, C. Huang, O. Cheng, Jpn. , *J. Appl. Phys*. **2011**, *50*, 04DC21.

[107] Y.S. Jeong, W.K. Oh, S. Kim, J. Jang, *Biomaterials*, **2011**, *32*, 7217.

[108] R. Loo, G. Wang, L. Souriau, J.C. Lin, S. Takeuchi, G. Brammertz, M. Caymax, *J. Electrochem. Soc*. **2010**, *157*, H13.

[109] J. Jang, B. Lim, *Angew. Chem. Int. Ed*. **2003**, *42*, 5600.

[110] J. Song, H. Song, H. Kong, J.-Y. Hong, J. Jang, *J. Mater. Chem.* **2011**, *21*, 19317.

[111] Y. Lin, Y. Liao, M. Weng, *Thin Solid Films*, **2009**, *517*, 5224.

국문초록

최근 들어 반도체 기술이 발달함에 따라 비용 절감을 위한 공정 미세화가 10 nm 수준까지 진행되었고, 앞으로도 회로의 선폭은 더욱 더 줄어들 전망이다. 이에 따라 기존에는 예상하지 못했던 문제가 새로이 발생하거나, 과거에 해결된 문제들이 다시금 문제가 되는 경우가 있다. 이러한 문제 중 하나가 바로 회로 사이의 절연과 수동태화에 사용되는 저유전물질의 부족한 물성이다. 저유전물질은 낮은 유전상수, 높은 기계적 물성, 낮은 흡습성, 고온에서의 안정성 등을 두루 갖춰야 하며 무엇보다도 수십 nm 급까지 좁아진 트렌치 격리의 내부에 결함과 빈틈이 없이 채워져야만 한다.

이를 위해 현재 다양한 저유전물질이 개발되어 사용되고 있다. 기존의 수백 nm 급 공정에서는 단순한 실리카가 사용되었고 실리카의 상대 유전상수(이하 유전상수)는 4 정도였다. 하지만 공정의 발달에 따라 낮은 유전상수를 가지는 저유전물질의 필요성이 커졌고, 그에 따라 유전상수값이 3 혹은 그 이하인 저유전물질이 개발되었다. 대표적으로 저유전물질로, 고분자 계열로는 폴리이미드, 다우 케미컬에서 생산되는 SiLK등이 있고, 유기실리카 계열의 퍼히드로폴리실라잔 등이 있다. 먼저 폴리이미드는 유전상수값 3정도를 가지며 화학적 기상증착으로 상대적으로 쉽게 제조할 수 있다는 장점을 가지나, 수분을 잘 흡수하는 문제가 있으며

좁은 트렌치 격리용으로 사용하기는 힘들다는 단점이 있다. 다우 케미컬에서 생산되는 SiLK의 경우는 2 전후 정도로 매우 낮은 유전상수를 가지지만, 기계적 물성이 약하다는 문제점이 있다. 마지막으로 퍼히드로폴리실라잔은 현재 20 nm 급 공정에서 실제로 사용되고 있으며 다양한 물리적 물성이 우수하나 가장 중요한 유전상수가 3 정도로 높다는 단점을 가지고 있다. 따라서 새로운 공정과 전구체를 통해 우수한 저유전막을 제조하는 것은 매우 중요하다.

메조기공 실리카는 50 nm 이하의 공극을 가지는 실리카로써 계면활성제를 통해 만들 수 있다. 만들어진 메조기공 실리카는 높은 표면적과 낮은 밀도를 가지며, 공극의 크기와 밀도의 조절을 통해 굴절률, 기계적 성능, 투과성 등을 조절할 수 있다. 이를 통해 약물전달시스템, 흡습제, 복합재료용 혼합제, 화장품, 코팅 등에 다양하게 응용될 수 있다. 그 중에서도 메조기공을 채우고 있는 공기의 유전율이 1 인 것을 이용, 저유전물질로써의 응용이 가능하다.

본 논문에서는 메조기공 실리카를 좁은 트렌치 내부에 기상으로 합성하여 이를 반도체용 저유전물질로 응용하는 것에 초점을 두고 있다. 기상증착중합을 통해 여러 가지 종류의 계면활성제와 다양한 전구체로 메조기공 실리카를 제조하였다. 만들어진 메조기공 실리카막은 저유전

물질로 응용되었고, 이를 통해 기계적 물성, 외형적 특성, 흡습성 등의 물성 변화 관찰과 최적화를 진행하였다.

주요어: 저유전물질, 메조기공 실리카, 유기실리카, 양이온계 계면활성제, 불소화 실리카, 영률, 흡습성

학번: 2009-21006